

## Intrinsic Properties of the $\langle z \rangle = 2.7$ Lyman Alpha Forest from Keck Spectra of QSO HS 1946+7658

DAVID KIRKMAN <sup>1</sup> and DAVID TYTLER <sup>2</sup>

Department of Physics, and Center for Astrophysics and Space Sciences  
University of California, San Diego  
MS 0111, La Jolla, CA 92093-0111

### ABSTRACT

We present the highest quality Ly $\alpha$  forest spectra published to date. We have complete 7.9 km s<sup>-1</sup> FWHM spectra between the Ly $\alpha$  and Ly $\beta$  emission lines of the bright, high redshift (V=15.9, z=3.05) QSO HS 1946+7658. The mean redshift of observed Ly $\alpha$  forest clouds is  $\langle z \rangle = 2.7$ . The spectrum has a signal to noise ratio per pixel of 2 km s<sup>-1</sup> that varies from 15 at 4190Å to 100 at 4925Å. The absorption lines in the spectrum have been fit with Voigt profiles, and the distribution of Voigt parameters has been analyzed. We show that fitting Voigt profiles to high quality data does not give unique results. We have performed simulations to differentiate between true features of the line distributions and artifacts of line blending and the fitting process. We show that the distribution of H I column densities is a power law of slope -1.5 from  $N(\text{H I}) = 10^{14} \text{ cm}^{-2}$  to  $N(\text{H I}) < 10^{12.1} \text{ cm}^{-2}$ . We further show that our data is consistent with the hypothesis that this power law extends to  $N(\text{H I}) = 0$ , because lines weaker than  $N(\text{H I}) = 10^{12.1} \text{ cm}^{-2}$  do not have a significant H I optical depth. At velocity dispersions between 20 and 60 km s<sup>-1</sup> the velocity dispersion ( $b$ ) distribution is well described by a Gaussian with a mean of 23 km s<sup>-1</sup>, and a  $\sigma_b$  of 14 km s<sup>-1</sup>. Very similar  $N(\text{H I})$  and  $b$  distributions were found at  $\langle z \rangle = 3.7$  by Lu et al. (1997), indicating no strong redshift evolution in these distributions for the Ly $\alpha$  forest. However, our  $b$  distribution has a lower mean and a wider dispersion than in past studies at the same redshift (eg. Hu et al. 1995) which had lower signal to noise spectra. We unambiguously see narrow

---

<sup>1</sup>dkirkman@ucsd.edu

<sup>2</sup>dtytler@ucsd.edu

Ly $\alpha$  forest clouds with  $14 \text{ km s}^{-1} \leq b \leq 20 \text{ km s}^{-1}$  that cannot be accounted for by noise effects. Our data also has absorption lines with  $b \geq 80 \text{ km s}^{-1}$  that can not be explained by the blending of lower  $b$  lines. We find that the lower cutoff in the  $b$  distribution varies with  $N(\text{H I})$ , from  $b = 14 \text{ km s}^{-1}$  at  $N(\text{H I}) = 10^{12.5} \text{ cm}^{-2}$  to  $b = 22 \text{ km s}^{-1}$  at  $N(\text{H I}) = 10^{14.0} \text{ cm}^{-2}$ . However, we see no similarly strong indication of a general correlation between  $b$  and  $N(\text{H I})$ . In contrast with previous results, we find no indication of Ly $\alpha$  forest line clustering on any scale above  $50 \text{ km s}^{-1}$ . Even among lines with  $10^{13.6} < N(\text{H I}) < 10^{14.3} \text{ cm}^{-2}$ , which were previously thought to cluster very strongly on velocity scales between 50 and  $150 \text{ km s}^{-1}$ , we see no clustering on any scale above  $50 \text{ km s}^{-1}$ , although we do see a  $3 \sigma$  clustering signal between 25 and  $50 \text{ km s}^{-1}$  among these higher column density lines. With the distributions we have derived, we have calculated the expected He II optical depth of the Ly $\alpha$  forest. If there are no lines with  $N(\text{H I}) < 10^{12.1} \text{ cm}^{-2}$ , the Ly $\alpha$  forest is unlikely to provide a significant portion of the He II optical depth at high redshift. However, if the distribution extends to  $N(\text{H I}) < 10^9 \text{ cm}^{-2}$ , the Ly $\alpha$  forest can provide all of the observed optical depth if  $N(\text{He II})/N(\text{H I}) \approx 100$ . We have calculated the redshift evolution of the optical depth from the He II Ly $\alpha$  forest based upon the line distributions we have derived for the H I Ly $\alpha$  forest. If the Ly $\alpha$  forest is responsible for the high redshift He II optical depth and the spectral shape of the UV background does not change with redshift, we predict  $\tau_{\text{HeII}} \approx 2.4$  at  $z = 3.3$  to be consistent with the value of  $\tau_{\text{HeII}}$  previously found at  $z = 2.4$ , provided that Ly $\alpha$  forest lines with  $N(\text{H I}) < 10^{13} \text{ cm}^{-2}$  evolve like those with  $N(\text{H I}) > 10^{13} \text{ cm}^{-2}$ .

## 1. Introduction

The numerous Ly $\alpha$  absorption lines found in the spectra of high redshift QSOs provide one of the few observational opportunities to study the high redshift universe. At low redshift, damped Ly $\alpha$  (DLA) and metal line absorption systems are known to be associated with galaxies (Lanzetta et al. 1995), and are believed to be at high redshift as well. The nature of the Ly $\alpha$  forest at high redshift is unknown, though they are believed to have an intergalactic origin. Traditionally the absorption was thought to occur in tenuous clouds confined either by pressure from a hot intergalactic medium (IGM) (Sargent et al. 1980), or by gravity (Melott 1980). However, recent cosmological simulations indicate that the Ly $\alpha$  forest may be composed of many different types of physical objects, including filaments of warm gas, velocity caustics, and collisionally ionized, high

density, hot gas (Cen and Ostriker 1993, Hernquist et al. 1996). A fluctuating H I Gunn-Peterson effect may also cause broad absorption features that would look like Ly $\alpha$  forest clouds (Miralda-Escude & Rees 1994).

### 1.1. Column Density Distribution

Many studies have attempted to determine the distribution functions which characterize the Ly $\alpha$  forest. The most recent (Hu et al. 1995) found the column density distribution to be of the form

$$\frac{dn}{dN} \propto N^{-1.46} \quad (1)$$

from  $N = 10^{12.3} \text{ cm}^{-2}$  to  $N = 3 \times 10^{14} \text{ cm}^{-2}$ , where  $N$  is the H I column density in  $\text{cm}^{-2}$  and  $n$  is the number of clouds per unit redshift. Previous studies have found similar results, but several found evidence for a break in the distribution in the vicinity of  $N = 10^{16} \text{ cm}^{-2}$  (Petitjean et al. 1993, and references therein). Line blending has prevented measurements of the distribution below  $N(\text{H I}) = 10^{12.3} \text{ cm}^{-2}$ .

### 1.2. Line Widths: Velocity Dispersion Distribution

The form of the line width velocity dispersion ( $b = \sqrt{2}\sigma_v$ ) distribution has been discussed in a number of recent papers. Pettini et al. (1990) reported that a majority of Ly $\alpha$  forest clouds have velocity dispersions  $b \leq 22 \text{ km s}^{-1}$  and that  $b$  is correlated with  $N(\text{H I})$ . Carswell et al. (1991) and Rauch et al. (1992) did not see a  $N(\text{H I})-b$  correlation in Q1100-264 and Q0014+813, respectively. Rauch et al. (1993) reanalyzed the original Pettini et al. spectrum of Q2206-199N and confirmed the appearance of both the very narrow lines and the  $N(\text{H I})-b$  correlation, but they performed simulations that showed both were probably artifacts of low signal to noise ratio (SNR). Hu et al. (1995) examined the  $b$  distribution of Ly $\alpha$  clouds in several objects and concluded that it was described by a Gaussian with mean of  $28 \text{ km s}^{-1}$ ,  $\sigma_b = 10 \text{ km s}^{-1}$  and a cutoff below  $20 \text{ km s}^{-1}$ . They agreed with the results of the Hernquist et al. (1996) simulations that the broad absorption features seen in spectra are blends composed of several narrower lines. Williger et al. (1994) and Lu et al. (1996) have also seen lines with  $b < 20 \text{ km s}^{-1}$ .

Low  $b$  lines, if real, challenge the conventional view that the Ly $\alpha$  forest clouds are hot and highly ionized. It is possible to obtain the low temperatures

implied by these  $b$  values –  $b = 20 \text{ km s}^{-1}$  is equivalent to 24,000 K – if the clouds are very dense,  $n_{\text{H I}} \approx 0.1 \text{ cm}^{-3}$  (Pettini et al. 1990). However, the inferred size of absorbers with this density ( $\approx 1 \text{ pc}$ ) is difficult to reconcile with the large sizes ( $\approx 100 h^{-1} \text{ kpc}$ ) inferred from absorption in the spectra of close QSO pairs (Smette et al. 1991, Dinshaw et al. 1995).

Other physical mechanisms which could produce low temperature Ly $\alpha$  forest clouds have been proposed. Ly $\alpha$  forest clouds can be cooled to low temperatures and still have a large size if they are adiabatically expanding against a confining force, perhaps gravity from dark matter halos or pressure from a hot IGM (Duncan et al. 1991). Further work on this model (Petitjean et al. 1993) has shown that the clouds are composed of shells of gas, with the high temperature gas toward the center of the cloud. For random lines of sight through the cloud, there is a 20 % chance of passing through a thin outer layer of the cloud with  $T < 15,000 \text{ K}$ , which corresponds to a  $b$  of at least  $15.7 \text{ km s}^{-1}$ ; where the observed  $b$  for such a cloud will be higher if there are turbulent motions. Giallongo and Petitjean (1994) have pointed out that clouds as large as 20 kpc can be cooled to about 20,000K ( $b = 18.1 \text{ km s}^{-1}$ ) by inverse Compton scattering of electrons on the cosmic microwave background. In the N-body cold dark matter simulations performed by Hernquist et al. (1996), most of the Ly $\alpha$  forest absorption occurs in structures with low temperatures ( $T \approx 20,000 \text{ K}$ ), and the apparent width of the lines is due entirely to the blending of many components.

### 1.3. Significance of the Ly $\alpha$ forest

Knowledge of the distributions which describe the Ly $\alpha$  forest cloud population is critical not only to understand the nature of the clouds themselves, but also to calibrate other astronomical observations. [D/H] measurements depend upon the line distributions to determine the likelihood that an H I line will masquerade as Deuterium in a given system (Tytler and Burles 1996). Understanding the column density distribution at low columns ( $N < 10^{12.5}$ ) is crucial in the interpretation of the recent measurements of the He II optical depth at high redshift (Jakobsen et al. 1994, Davidsen et al. 1996). If there are a large number of absorbers with  $N < 10^{12.5} \text{ cm}^{-2}$ , Ly $\alpha$  forest clouds can account for all of the observed He II absorption for expected values of [He II/H I], without any need for additional Gunn-Peterson absorption. In a broader sense, it now appears that most baryons are in the structures which show Ly $\alpha$  forest absorption (Meiksin and Madau 1993, Rauch et al. 1997, Weinberg et al. 1997). Comparison of the observed forest with the results of

computer simulations constrain the cosmological baryon density,  $\Omega_b$ , and also the thermal and ionization history of the universe on the largest scales.

All wavelengths presented in this paper are vacuum values, and all observed wavelengths have been reduced to the solar rest frame. We use  $H_0 = 100h$   $\text{km s}^{-1} \text{Mpc}^{-1}$ .

## 2. Observations and Extraction

In July 1994, we used the HIRES spectrograph (Vogt 1994) on the Keck Telescope to take seven spectra of QSO HS 1946+7658 ( $V=15.9$ ,  $Z=3.051$ ) discovered in the Hamburg Survey (Hagen et al. 1992). We selected this object because it is the brightest high redshift QSO known. All seven observations were made during good seeing conditions, with a  $1.148''$  slit, the C5 decker, and  $1 \times 2$  on-chip binning (along the slit) on a Tex 2048 CCD. The total integrated time on the object was 13.3 hours. We have complete wavelength coverage between the  $\text{Ly}\alpha$  and  $\text{Ly}\beta$  emission lines. The spectra were optimally extracted and wavelength calibrated using the EE package written by Tom Barlow. Once extracted, the individual spectra were rebinned onto a common linear wavelength scale, and combined using weights to form a composite spectrum. The resulting spectrum has a SNR per pixel ( $\approx 0.031 \text{ \AA}$ ) that varies from 15 at  $4190 \text{ \AA}$  to 100 at  $4925 \text{ \AA}$ . The SNR also varies across each echelle order, being a factor of  $\approx 1.5$  greater in the center of the order than at the edges. The resolution of the spectrum is  $7.9 \text{ km s}^{-1}$ . The spectrum was not fluxed to an absolute energy scale. A preliminary local continuum level was obtained independently for each echelle order by identifying regions in the spectrum unaffected by absorption features and interpolating between them with a seventh order Legendre polynomial, which provide good fits to the continuum level in the echelle orders redward of  $\text{Ly}\alpha$  emission, where there is little absorption. The spectrum between the  $\text{Ly}\alpha$  and  $\text{Ly}\beta$  emission lines is displayed in Figure 1.

A DLA line that fell between two orders of the echelle image prevented us from obtaining an accurate continuum level and line profiles in the region between  $4664 \text{ \AA}$  and  $4721 \text{ \AA}$ . This region of the spectrum is not included in Figure 1, and none of the lines in that region have been included in any of our analysis. We do not discuss the DLA, which has been extensively studied by others (Fan & Tytler 1994, Lu et al. 1995). Two regions of the spectrum presented in Figure 1 have not been fit with Voigt profiles. The region between  $4635 \text{ \AA}$  and  $4640 \text{ \AA}$  is believed to contain both  $\text{Ly}\alpha$  forest lines and Si III (1206.5) from the  $z = 2.84$  DLA system. Because it is heavily blended and we

have no other Si III transition available to guide us in fitting, we have excluded the region from our analysis. No data was obtained near 4300.5 Å because of the ink spot on the HIRES CCD.

### 2.1. Fitting Line Parameters

We used Carswell’s VPFIT software to fit all of the absorption features with Voigt profiles. The Voigt parameters and identifications for each absorber in the spectrum are listed in Table 1. We broke the spectrum up into the smallest possible absorption regions, bounded where the spectrum reached the continuum level. Initial line parameters (guesses) for each region were set by hand and given to VPFIT, which adjusts the initial parameters to minimize the  $\chi^2$  between the fit and the data. We added lines until we obtained a reduced  $\chi^2$  between fit and data of less than 1.3 over the region being fit, and we always attempted to use the fewest number of lines capable of meeting this condition.  $P(\chi^2)$ , the probability of good fit being rejected because of extreme noise fluctuations, is between 1% and 10% for  $\chi^2 < 1.3$ , depending upon the number of lines and the size of the region being fit.

Because the local continuum level is not well determined in the Ly $\alpha$  forest, we adjusted the continuum level in each order to give an optimum fit between the data and the calculated Voigt profiles. The continuum level of each order was taken to be a Legendre polynomial – adjustments of the continuum level were made by changing the coefficients of the polynomial. The polynomial describing each order was constrained to be of order seven or less.

The Voigt profiles obtained by this fitting procedure may not accurately describe the absorbing gas. For example, several discreet clouds located tens of kpc apart, each with a small  $b$  value, may blend together in the spectrum and appear in the line list as a single localized cloud with a high  $b$  value. This ambiguity complicates the process of determining the physical properties of the absorbing gas. However, the VPFIT procedure usually results in a consistent description of the spectra and is universally used (Carswell et al., 1984). Unfortunately, it does not always yield unique results. (Section 3.2)

### 2.2. Metal Lines

We have attempted to identify all of the metal lines present in the Ly $\alpha$  forest. We began by searching for C IV (1548.195, 1550.770) doublets, both in and out of the forest. We also searched for any line associated with known

absorption systems identified redward of the forest (e.g. the DLA systems at  $z = 2.844$  and  $z = 1.738$ ), as well as for the Si IV (1393.755, 1402.770) and Mg II (2796.352, 2803.531) doublets. This method identified all of the metal line systems previously in the literature (Fan and Tytler 1994, Lu et al. 1995) as well as several new systems (C IV systems at  $z_{\text{abs}} = 2.228, 2.465, 2.499, 2.985,$  and  $3.027$ ). All absorption lines short of Ly $\alpha$  emission at 4924 Å were assumed to be Ly $\alpha$  unless we found other identifications. Because many of the lines in the forest are blended, line wavelengths have a much greater uncertainty than they do outside of the forest and we may have misidentified a few metal lines as Ly $\alpha$ .

### 3. Absorption Line Parameters

#### 3.1. Line Blanketing and Blending

We must distinguish between an observed distribution obtained by fitting Voigt profiles to absorption features in a spectrum, and an intrinsic distribution that describes the physical state of the gas responsible for the absorption. The two are different because of line blanketing and line blending.

Line blanketing occurs when a weak line is located in the absorption profile of a stronger line, and as a result is not observed. The stronger line does not have to be saturated to effectively blanket weaker lines. Line blanketing decreases the observed number of low column density lines.

Line blending occurs when two lines can not be resolved and are instead fit with a single Voigt profile. The effect of line blending is to create a higher proportion of wide lines than is present in the intrinsic distribution. Both effects decrease with increasing SNR.

#### 3.2. Non-uniqness of fitted Line Parameters

The process of fitting Voigt profiles to absorption spectra can not yield unique results. Examples of this are shown in Figure 2, where we show two different sets of Voigt profiles which fit each absorption feature. In both cases, although one of the solutions is better than the other, both meet our criterion for a satisfactory fit. The reduced  $\chi^2$  for the region shown in each panel is as follows: Panel A – 0.83, Panel B – 1.15, Panel C – 1.04, Panel D – 1.16. The differences between line parameters in the different solutions are far greater than the formal fitting errors for those parameters. We do not have the resources to systematically search all of parameter space during the fitting process, and

in general we accept the first satisfactory solution found. As can be seen in Figure 2, this solution can be distant in parameter space from better (lower  $\chi^2$ ) solutions.

We do not believe that the fitting process can be made more unique by lowering the  $\chi^2$  acceptance threshold.  $P(\chi^2)$ , the probability that random noise will cause the fit to be rejected is between 1% and 10% (depending upon the size of the region being fitted and the number of lines in the fit) for our  $\chi^2$  threshold of 1.3. If noise causes the fit to be rejected, more lines, usually heavily blended, will be added. If we attempt to combat the non-uniqueness of the fitting process by lowering the acceptable  $\chi^2$  for a fit, we will systematically increase the number of lines observed in the spectrum, and because most of the additional lines will be heavily blended, they are not likely to be well determined, and the new solution will be less unique.

The observed distribution functions for the H I Ly $\alpha$  forest towards QSO HS 1946+7658 can be obtained directly from Table 1, and are shown in Figures 3, 4, 5, and 6. The intrinsic distributions are more interesting because they must be used when comparing different observations or when comparing observation with theory. The observed distributions obtained from different observations should not be directly compared with each other because they depend upon both the SNR of the data and the details of the process used to fit Voigt profiles to the data, among other things.

Unfortunately, it is not possible to invert the problem and compute the intrinsic line distribution responsible for the absorption spectrum from an observed distribution and the details of the observation. With the aid of simulations, however, it is possible to determine intrinsic distributions from observed distributions.

Throughout the rest of the paper we will be talking about three types of distribution. An intrinsic distribution describes the physical state of the absorbing gas – either in reality or as assumed for a simulation. An observed distribution is derived from lines fit to real QSO absorption line spectra. Simulated-observations give distributions that have been derived from simulated spectra, which we treated like the real spectra.

### 3.3. Simulations and the Intrinsic Line Distributions

We have performed simulations to determine the intrinsic distributions of the Ly $\alpha$  forest lines in our spectrum. A simulated-observation consists of creating an artificial spectrum from a given intrinsic distribution, and then



fitting the artificial data in the same manner as the real data. The intrinsic  $N(\text{H I})$  and  $b$  distributions we used were the distributions Hu et al. (1995) found to describe the  $\text{Ly}\alpha$  forest. (See sections 3.4 and 3.5 for details). We attempted to mimic every systematic aspect of the real spectra. The artificial spectrum was convolved with a Gaussian to simulate the  $7.9 \text{ km s}^{-1}$  resolution of the real data. It was broken up into echelle orders at the same wavelength boundaries as the real data. Of the 13 echelle orders observed towards HS 1946+7658, 10 were simulated. For each order in the real spectrum, we fit the noise array with a 4'th order Legendre polynomial and then added noise to the simulated data at the level of the smoothed noise array. Voigt profiles were fit to the simulated spectra with the same procedure used to fit the real spectra. The simulated spectra was not continuum fit as the real data, because the continuum errors in the real spectrum are not known. Since continuum errors are likely to show up as lines with very high velocity dispersions ( $b > 100 \text{ km s}^{-1}$ ), the simulated-observations may not yield the correct intrinsic distribution of such lines.

### 3.4. $N(\text{H I})$ Distribution

We find the intrinsic  $N(\text{H I})$  distribution per unit redshift to be

$$\frac{dn}{dN} = \begin{cases} 0 & N < N_{min} \\ 6.2 \times 10^8 N^{-1.5} & N \geq N_{min} \end{cases} \quad (2)$$

with  $N_{min} < 10^{12.1} \text{ cm}^{-2}$ . The  $N(\text{H I})$  distribution observed towards HS 1946+7658 is shown in Figure 3. All observed  $\text{Ly}\alpha$  lines (including those associated with metal line systems) were used to determine this distribution. The mean redshift of these observations is 2.7.

The  $N(\text{H I})$  distribution from the simulated-observations is shown in Figure 7. The intrinsic distribution used to make the simulation is given by Equation 2, with  $N_{min} = 10^{12.0} \text{ cm}^{-2}$ . This is similar to the  $N(\text{H I})$  distribution used by Hu et al. (1995), but we have adjusted the normalization to give the number of lines that we observed at  $N(\text{H I}) < 10^{13} \text{ cm}^{-2}$ . Figures 3 and 7 are the same to within error bars, so we conclude that intrinsic distribution of the  $\text{Ly}\alpha$  forest clouds is given by Equation 2. The simulated-observations indicate that the entire fall off seen in Figure 3 is expected from line blanketing, and that our line list is complete for  $N(\text{H I}) > 10^{13} \text{ cm}^{-2}$ .

Because the low end of the  $N(\text{H I})$  distribution can have a significant or even dominant effect upon the mean He II optical depth of the  $\text{Ly}\alpha$  forest clouds, we

wish to determine the maximum  $N_{min}$  that is consistent with our observations. We performed a number of different partial simulations, corresponding to orders 74 and 73 in the spectrum of HS 1946+7658, with N(H I) distributions characterized by different  $N_{min}$ . Orders 74 and 73 cover the wavelength region from 4783 Å to 4919 Å. We only performed partial simulations so that we could perform many in a reasonable time, and we simulated orders 74 and 73 because they had the highest SNR and hence the most low N(H I) lines. The results of these simulations indicate that any  $N_{min}$  below  $10^{12.1} \text{ cm}^{-2}$  is acceptable. Any value of  $N_{min}$  above  $10^{12.1} \text{ cm}^{-2}$  results in simulated-observations that contain too few lines with  $N(\text{H I}) < 10^{12.1} \text{ cm}^{-2}$ . If  $N_{min}$  is set below  $10^{12.1} \text{ cm}^{-2}$ , the H I optical depth of the additional lines is so low that they have no effect upon the observed distribution for data with our SNR levels. In Figure 8 we show both the mean H I absorption of the Ly $\alpha$  forest at a redshift of 2.7 for different values of  $N_{min}$ , as well as the mean differential absorption of the H I Ly $\alpha$  forest per unit column density. Note that most of the H I Ly $\alpha$  forest opacity occurs in clouds with  $10^{13} < N(\text{H I}) < 10^{15} \text{ cm}^{-2}$ , and that the differential contribution to the Ly $\alpha$  opacity is a maximum at  $N(\text{H I}) = 10^{14} \text{ cm}^{-2}$ . Also note that the contribution to  $D_A$ , the mean drop below the continuum level due to Ly $\alpha$  absorption, from lines below  $N(\text{H I}) = 10^{12.1} \text{ cm}^{-2}$  would be less than 2 %.

It is physically reasonable for the N(H I) distribution to extend to  $N(\text{H I}) = 10^{12.1} \text{ cm}^{-2}$ . If the distribution of column densities is given by Equation 2, the mean proper distance between a Ly $\alpha$  forest cloud and it's nearest neighbor with  $N(\text{H I}) \geq N_0$  is given by (in a  $\Omega = 1$ ,  $q_0 = 0.5$  cosmology)

$$d = 100h_{100}^{-1} \left( \frac{N_{min}}{10^{12.07}} \right)^{\frac{1}{2}} \text{ kpc.} \quad (3)$$

If the size of the all of the Ly $\alpha$  forest clouds is  $100h^{-1} \text{ kpc}$ , the filling factor of the Ly $\alpha$  forest approaches unity when  $N_{min} \approx 10^{12.1} \text{ cm}^{-2}$ .

### 3.5. $b$ Value Distribution

We made simulated spectra from the intrinsic distribution that Hu et al. (1995) found to describe the Ly $\alpha$  forest: a Gaussian with a mean of  $28 \text{ km s}^{-1}$  and  $\sigma_b = 10 \text{ km s}^{-1}$ . The  $b$  distribution from the simulated-observations for lines with  $N(\text{H I}) > 10^{12.5} \text{ cm}^{-2}$  is shown in Figure 9. The simulated-observations clearly resemble the intrinsic distribution, but there are significant differences between the two. Primarily, there is a tail of wide  $b$  lines in the simulated-observations that were not present in the intrinsic distribution – these are the

lines in the “hump” seen in the  $N(\text{H I})$ - $b$  distribution between  $10^{12.5} < N(\text{H I}) < 10^{13.5} \text{ cm}^{-2}$  (See section 3.6). The simulated-observations are not a Gaussian, but if we force a Gaussian fit upon the region between  $b = 20$  and  $b = 60 \text{ km s}^{-1}$  we find a mean of  $29 \text{ km s}^{-1}$  and a  $\sigma_b$  of  $9 \text{ km s}^{-1}$ , which is nearly identical to the intrinsic distribution used to make the simulation.

The simulated-observations look a lot like the real observations, except that the position of the peak of the  $b$  distribution occurs at a significantly lower  $b$  value in the real observations. This means that the intrinsic  $b$  distribution used to create the simulated-observations is not the intrinsic  $b$  distribution of the real data. We wish to determine the intrinsic  $b$  distribution of the real data, but the only true way to do this is guess the correct intrinsic distribution, perform simulations, and then see that the simulated-observations are the same as the real observations. Unfortunately, simulations are extremely expensive to perform.

To avoid performing more simulations, we have simply noted that if we fit the  $b$  distribution from the simulated-observations between 20 and  $60 \text{ km s}^{-1}$  with a Gaussian, we get a result that closely resembles the intrinsic distribution used to create the simulation. In short, the simulated-observations indicate that the observed  $b$  distribution will closely resemble the intrinsic distribution. However, due to line blending, the observed distribution will have a tail of high  $b$  lines that is not present in the intrinsic distribution. The simulations performed by Hu et al. (1995) and Lu et al. (1997) displayed the same behavior.

If we do the same thing to our observed  $b$  distribution – that is fit it with a Gaussian between  $b = 20$  and  $b = 60 \text{ km s}^{-1}$ , we get a mean for the Gaussian of  $23 \text{ km s}^{-1}$  and a  $\sigma_b$  of  $14 \text{ km s}^{-1}$ . As was the case for the simulated-observations, this Gaussian does not fit the observed distribution perfectly. However, based upon the results of the simulated-observations we believe that this is close to the actual intrinsic  $b$  distribution for the  $\text{Ly}\alpha$  forest. Without further simulations we will not be able to determine the exact form of the intrinsic  $b$  distribution, but for the purposes of this paper it is sufficient to know that it is close to a Gaussian with a mean of  $23 \text{ km s}^{-1}$  and a  $\sigma_b$  of  $14 \text{ km s}^{-1}$ . The mean  $b$  is lower and the  $\sigma_b$  is larger than found by Hu et al. (1995) with lower SNR data. We do not know whether the difference comes from the data, simulations, or the fitting.

There is a significant non-Gaussian tail to the  $b$  distributions from both the real data and the simulated-observations. In the case of the simulated-observations, it is due entirely to line blending. Consequently, line blending must create a tail in the observed distribution as well, although the observed tail may contain more lines than we would expect pure line blending. 3.4 %

(16 of 466) of the lines observed towards HS 1946+7658 have  $b > 80 \text{ km s}^{-1}$ , whereas only 0.5 % (2 of 363) of the lines in the simulated-observations have  $b > 80 \text{ km s}^{-1}$ . The extra lines may be indicative of a non-Gaussian tail that is present in the intrinsic  $b$  distribution. Unfortunately, we would have to make new simulations with a mean of  $23 \text{ km s}^{-1}$  and a  $\sigma_b$  of  $14 \text{ km s}^{-1}$  to verify this. Some of the high  $b$  lines could be removed from the spectrum with a high order continuum (Legendre polynomial of order  $\geq 15$ ), but we chose not to do this because the continuum levels of the 16 red orders in this spectrum which have no Ly $\alpha$  absorption are all well fit by seventh order Legendre polynomials.

Physically, an intrinsic population of high  $b$  Ly $\alpha$  lines could represent high temperature gas ( $10^6 \text{ K}$ ) such as is found in the halos of galaxies. If these lines are hot Ly $\alpha$  clouds, they may show high ionization metals such as O VI, Ne VIII, Mg X or Si XII (Verner, Tytler, & Barthel 1994). At such high temperatures we do not expect to see strong C IV absorption, which reaches its maximum abundance at  $T=1.1 \times 10^5 \text{ K}$ , and begins to decrease rapidly at higher temperatures. We do not have high enough SNR at blue wavelengths to see O VI in this spectrum.

### 3.6. N(H I) - $b$ Distribution and the lower cutoff in the $b$ distribution

We have found a correlation between the lowest  $b$  values and N(H I). In Figure 5 we have plotted N(H I) vs.  $b$  for the Ly $\alpha$  lines observed towards HS 1946+7658. The correlation between the lowest  $b$  values, denoted  $b_{min}$ , and N(H I) is easily seen among the lines with  $N(\text{H I}) > 10^{12.5} \text{ cm}^{-2}$ , and is approximately given by the line

$$b_{min} = 14 + 4 \times \text{Log} \left( \frac{N(\text{H I})}{10^{12.5}} \right) \text{ km s}^{-1}, \quad (4)$$

which is shown in Figure 5. This correlation between  $b_{min}$  and N(H I) was not present in the simulated-observations, which are plotted in N(H I) vs.  $b$  format in Figure 10. The intrinsic distribution used in the simulated-observations had a lower cutoff of  $20 \text{ km s}^{-1}$ , which was perfectly preserved in the simulated-observations for lines with  $N(\text{H I}) > 10^{12.5} \text{ cm}^{-2}$ . Because the lower cutoff in the simulated-observations was so well preserved for these lines we believe that Equation 4 represents a correlation present in the real intrinsic distribution.

Note that the N(H I)- $b$  distribution from the simulated-observations is very similar to the observed N(H I)- $b$  distribution. Both show a “hump” containing

a number of wide  $b$  lines between  $N(\text{H I}) = 10^{12.5}$  and  $10^{13.5} \text{ cm}^{-2}$ , and a number of low  $b$  lines with  $N(\text{H I}) < 10^{12.5} \text{ cm}^{-2}$ . Also note that the intrinsic distribution used to create the dataset from which the simulated observations were made (Figure 11) is essentially featureless.

There are three conspicuous lines in Figure 5 which lie below  $b = 20 \text{ km s}^{-1}$  and above  $N(\text{H I}) = 10^{12.5} \text{ cm}^{-2}$ . We suspect that these lines may be unidentified metals, but we can not positively identify them because  $\text{Ly}\alpha$  forest absorption may be blanketing other transitions. Possible non- $\text{Ly}\alpha$  identifications for the lines are as follows. The line at  $4190.2 \text{ \AA}$  is definitely not part of any of the C IV (1548.195, 1550.77), SiIV (1393.755, 1402.77) or N V (1238.821, 1242.804) doublets, it could be either Mg II (2796.352) or Al III (1854.716). The line at  $4176.9 \text{ \AA}$  is not part of the C IV (1548.195, 1550.77), or N V (1238.821, 1242.804) doublets, it could be Mg II (2796.352), Mg II (2803.531), Al III (1854.716) or Al III (1862.79). The line at  $4293 \text{ \AA}$  could be C IV (1548.195). However, all three lines appear as  $\text{Ly}\alpha$  in our line list.

We see twice as many lines with  $b < 20 \text{ km s}^{-1}$  and  $N(\text{H I}) < 10^{12.5} \text{ cm}^{-2}$  in the observed distribution as we did in the simulated-observations, indicating that any cutoff present in the  $b$  distribution for lines with  $N(\text{H I}) < 10^{12.5}$  is below  $20 \text{ km s}^{-1}$ . This is what we expect if Equation 4 is extrapolated below  $N(\text{H I}) = 10^{12.5} \text{ cm}^{-2}$ . This region contains 10 % of the observed lines, compared to 4.7 % in the simulated-observations, which used a lower cutoff in the intrinsic  $b$  distribution of  $20 \text{ km s}^{-1}$ . The 4.7 % must be noise features because there were no lines with  $b < 20$  put into the simulation. The formal fitting errors are not large enough (typically  $\approx 20\%$  in  $b$ ) to explain the excess. The remaining 5.3 % are apparently real. Rauch et al. (1992) first realized while reanalyzing the spectrum of Q2206-199N that the observed distribution will contain low  $b$  lines at low  $N(\text{H I})$  (relative to the quality of the data) that are not present in intrinsic distribution.

While the correlation we see between  $b_{min}$  and  $N(\text{H I})$  is reminiscent of the correlation between  $b$  and  $N(\text{H I})$  found by Pettini et al. (1990), it is not the same. The correlation reported by Pettini et al. (1990) was a general correlation between every observed  $b$  and every observed  $N(\text{H I})$ , a correlation that is easily seen in the observed distribution of HS 1946+7658, and in the distribution from the simulated-observations. The correlation in the low SNR data was later shown by Rauch et al. (1993) to be an artifact of the fitting process, a conclusion that we verify. The origin of this correlation can be seen from the simulated-observations, where it occurs for two reasons: there are a large number of high  $b$  lines with  $10^{12.5} < N(\text{H I}) < 10^{13.5} \text{ cm}^{-2}$  (due to line blending),

and a large number of low  $b$  lines with  $N(\text{H I}) < 10^{12.5} \text{ cm}^{-2}$ . We do not understand the mechanism that produces low  $b$  lines below  $10^{12.5} \text{ cm}^{-2}$ . They are not all pure noise features because their SNR is too high (a  $N(\text{H I}) = 10^{12} \text{ cm}^{-2}$  line has an equivalent width of 20 mÅ at  $z = 2.7$ , which is about a  $5 \sigma$  event for our data.) However, because they appear in the simulated-observations we know that the observed distribution contains lines like this that are not part of the intrinsic distribution.

While we see no general intrinsic correlation between  $N(\text{H I})$  and  $b$ , we are reporting a correlation between the very lowest  $b$  values and  $N(\text{H I})$  that is present in the observed distribution and in the intrinsic distribution. And this correlation, along with the fact that the very narrowest lines have  $b$  values between 14 and 20  $\text{km s}^{-1}$ , raises the same issues originally brought up by Pettini et al (1990). How is it that lines can obtain  $b$  values of  $< 20 \text{ km s}^{-1}$ , and why should there be a correlation between the very smallest  $b$  values and  $N(\text{H I})$ ?

There is (at least) one mechanism that can cool a  $\text{Ly}\alpha$  forest cloud to 14  $\text{km s}^{-1}$ . In the adiabatically expanding  $\text{Ly}\alpha$  cloud model discussed by Duncan, Vishniac & Ostriker (1991) and refined by Petitjean et al. (1993), the  $\text{Ly}\alpha$  clouds are adiabatically expanding against pressure from the IGM. Detailed calculations with this model (Petitjean et al. 1993) show that parts of such an expanding cloud will have temperatures that fall below  $b = 20 \text{ km s}^{-1}$ , though no part of such a cloud will fall below 10  $\text{km s}^{-1}$ . Because the edges of the clouds are cooler, there will be a correlation between column density and temperature, which may explain the correlation seen between  $b_{min}$  and  $N(\text{H I})$ . Different lines a sight through a particular cloud type (key parameters are the central density of the cloud and it's expansion velocity) trace out a curve in the  $N(\text{H I}) - b$  plane, with a positive correlation between  $N(\text{H I})$  and  $b$ . The many different cloud types required for consistency with global  $\text{Ly}\alpha$  cloud properties make it extremely difficult for this model to explain an overall general correlation between  $N(\text{H I})$  and  $b$  (such as was reported by Pettini et al., but later shown to be an artifact of the line fitting process by Rauch et al.) but a correlation between  $b_{min}$  and  $N(\text{H I})$  might be achievable, and would correspond to different lines of sight through a cloud type with maximal central density and expansion velocity.

Clouds may also cool by inverse Compton scattering of electrons on the cosmic microwave background (Giallongo and Petitjean 1994), but their calculations indicate that this will only cool  $\text{Ly}\alpha$  forest clouds to 18.1  $\text{km s}^{-1}$ .

Of course, the correlation between  $b_{min}$  and  $N(\text{H I})$  may simply be indicating

that clouds with larger  $N(\text{H I})$  are more turbulent. However, it is hard to see why this would lead to such a sharp lower limit in the  $b$  distribution, it does not explain how the lines below  $N(\text{H I}) = 10^{14} \text{ cm}^{-2}$  cool below  $20 \text{ km s}^{-1}$ , and it should lead to a general correlation between  $N(\text{H I})$  and  $b$ , which we do not see. A similar correlation between  $b_{min}$  and  $N(\text{H I})$  has been seen in hydrodynamical CDM simulations performed by Zhang, Anninos, and Norman (1995).

### 3.7. Possible Metal Line Contamination of Ly $\alpha$ Line List

There are not enough unidentified metal lines in our line list to have significantly affected any part of the  $b$  distribution with measured columns greater than  $10^{12.5} \text{ cm}^{-2}$ . In particular, there are many more narrow lines in our line list than can be accounted for by unidentified metals.

We can compare, per unit redshift, the number of metal lines inside and outside the forest. The lines outside of the forest are trivial to identify – any absorption seen is a metal line. In general, a metal line system will require more components to fit if it has been observed with higher SNR. Because the orders of our HS 1946+7658 spectra outside of the Ly $\alpha$  forest have much higher SNR than many of the orders inside the Ly $\alpha$  forest, we can not simply compare the number of metal lines inside and outside of the forest. Instead we count groups of lines.

We define a narrow line cluster as a group of one or more narrow lines ( $b < 20$  and  $N(\text{HI}) > 12.5$ ) grouped within  $250 \text{ km s}^{-1}$ , the scale on which metal lines are known to cluster. We found 74 clusters (254 narrow lines) in a wavelength interval of  $1370 \text{ \AA}$  above the Ly $\alpha$  forest, all of which must be metals. We would hence expect to find 37 metal line clusters inside of the Ly $\alpha$  forest: we found 21 (65 lines). We additionally found 35 clusters (47 lines) which we believe to be Ly $\alpha$ .

This would indicate that half of the narrow lines we have identified as Ly $\alpha$  may be metal lines. However, we believe that most of the 47 narrow lines identified as H I Ly $\alpha$  are H I for three reasons. First, we expect that many of the narrow metal lines present inside of the Ly $\alpha$  forest have been blanketed because many of the metal lines outside of the forest are weak when compared with Ly $\alpha$  forest lines. Second, the narrow lines we have identified as Ly $\alpha$  cluster much less strongly on a  $250 \text{ km s}^{-1}$  scale than the lines we have identified as metals (3.1 lines per cluster for identified metal lines vs 1.3 for assumed Ly $\alpha$ ). Third, we did not find identifications for the narrow Ly $\alpha$  cluster lines, even though we have coverage to C IV and the highest SNR to date.

#### 4. Implied He II optical depth of the Ly $\alpha$ forest

Using the distribution functions we have found for the H I Ly $\alpha$  forest, we can calculate the expected He II optical depth of the Ly $\alpha$  forest as a function of  $N(\text{He II})/N(\text{H I})$ . The He II optical depth at  $z = 2.4$  and  $z = 3.3$  has been measured towards three high redshift QSOs (Jakobsen et al. 1994, Davidson et al. 1996, Tytler & Jakobsen (unpublished)). Since we wish to compare the expected He II optical depth of the Ly $\alpha$  forest with the observations, we will have to take into account the redshift evolution of the Ly $\alpha$  forest. We will assume that the  $b$  and  $N(\text{H I})$  distributions remain unchanged with redshift, and that the normalization of the  $z$  distribution evolves like

$$\frac{dn}{dz} \propto (1+z)^{2.6}. \quad (5)$$

This is the redshift evolution found by Cristiani et al. (1995), for H I Ly $\alpha$  forest lines with  $N(\text{H I}) > 10^{13} \text{ cm}^{-2}$ . Because the  $N(\text{H I})$  distribution we found (at  $\langle z \rangle = 2.7$ ) agrees with the  $N(\text{H I})$  distribution found by Lu et al. (1997) above  $N(\text{H I}) = 10^{12.3} \text{ cm}^{-2}$  at  $\langle z \rangle = 3.7$  (Lu et al. (1997) provided no information about lower column lines), we know that lines with  $N(\text{H I}) > 10^{12.3} \text{ cm}^{-2}$  have the same redshift evolution. There is no information available on the evolution of lines with  $N(\text{H I}) < 10^{12.3} \text{ cm}^{-2}$ , so we will assume that they evolve like the lines with  $N(\text{H I}) > 10^{12.3} \text{ cm}^{-2}$ . An example of simulated He II Ly $\alpha$  forest spectra at  $7.9 \text{ km s}^{-1}$  is shown in Figure 12.

To calculate the optical depth of the He II Ly $\alpha$  forest, we have to specify how much of the H I  $b$  value is thermal. We have done the calculation twice: once assuming that the H I  $b$  value is entirely thermal, and once where 10  $\text{km s}^{-1}$  of the H I  $b$  value is thermal with the rest turbulent. These two scenarios represent opposite extremes in the possible  $b$  values for He II Ly $\alpha$  lines – there is no known way to cool an H I Ly $\alpha$  forest line below  $10 \text{ km s}^{-1}$ .

The results of these calculations, with the  $N(\text{H I})$  distribution cut at below  $10^{12.1} \text{ cm}^{-2}$ , are presented in Figure 13. In this case, the Ly $\alpha$  forest can account for all of the observed He II absorption at  $z = 2.4$  when  $N(\text{He II})/N(\text{H I}) \approx 10^3$  to  $10^4$ , depending upon how much of the H I  $b$  value is thermal. These values are much larger than expected from common models of the UV background radiation (Miralda-Escude 1993b), but are not unreasonable if there is a large break in the UV spectrum at the  $228 \text{ \AA}$  He II edge.

However, as pointed out by Songaila et al. (1995), if  $N_{\text{min}} < 10^{12.1}$  the Ly $\alpha$  forest can account for all of the observed He II absorption for much smaller values of  $N(\text{He II})/N(\text{H I})$ . In Figure 14, we present the results of a calculation



of  $\tau_{\text{HeII}}$  with  $N_{\text{min}} = 9.0$  (effectively zero). In this case,  $N(\text{He II})/N(\text{H I})$  needs only be  $\approx 100$  to  $\approx 150$  for the Ly $\alpha$  forest to account for all of the observed He II optical depth at  $z = 2.4$ . The difference between thermal and turbulent H I  $b$  values is now less significant because unsaturated lines are now responsible for a much larger fraction of the  $\tau_{\text{HeII}}$ .

We would like to determine how much of the high redshift He II optical depth is due to the Ly $\alpha$  forest, because we would then know how much is due to the IGM (insomuch as any optical depth not due to the forest must come from the IGM, i.e. the Gunn-Peterson effect). Unfortunately, after viewing both Figure 13 and Figure 14, it becomes clear that it is entirely possible for the Ly $\alpha$  forest to be responsible for all of the observed high redshift He II optical depth, or a small fraction of it (or anywhere in between). To ultimately determine the He II optical depth of the Ly $\alpha$  forest, we will have to determine  $N(\text{He II})/N(\text{H I})$  in the forest (probably via observations the He II lines of Ly $\alpha$  forest clouds). We will also have to determine  $N_{\text{min}}$  or place a limit on it that is less than  $10^9 \text{ cm}^{-2}$ , as well as the redshift evolution of the low  $N(\text{H I})$  lines. Determining  $N_{\text{min}}$  will be extremely difficult.

In any event, unless  $N(\text{He II})/N(\text{H I})$  is much lower than expected,  $\tau_{\text{HeII}}$  will be dominated by either the IGM or low  $N(\text{H I})$  Ly $\alpha$  forest clouds. The redshift evolution of  $\tau_{\text{HeII}}$  will hence give the redshift evolution of either low  $N(\text{H I})$  Ly $\alpha$  forest clouds, the IGM, or a combination of both.

Since the number of observed lines per  $\text{\AA}$  of spectrum increases like  $(1+z)^{2.6}$  (Equation 5), and the equivalent width of each line goes as  $(1+z)$ , we expect that the redshift evolution of the He II optical depth from Ly $\alpha$  forest clouds to be given by

$$\tau(z)_{\text{HeII}} \propto (1+z)^{3.6}. \quad (6)$$

The calculations in Figures 12 and 13 indicate that this is indeed the case and that the blanketing effects of saturated He II lines do not strongly effect the redshift evolution of the Ly $\alpha$  forest  $\tau_{\text{HeII}}$ .

The key point is that the redshift evolution of the Ly $\alpha$  forest He II optical depth is dominated by the number of lines present at any redshift. It does not depend upon whether or not the H I  $b$  values are thermal. It does not depend upon  $N(\text{He II})/N(\text{H I})$  (it does depend upon any change of  $N(\text{He II})/N(\text{H I})$  with redshift). It does not depend upon the form of the  $N(\text{H I})$  distribution below  $10^{13} \text{ cm}^{-2}$ . Hence if  $\tau_{\text{HeII}}$  is found not to have the redshift evolution found in Equation 6, either the IGM or the low  $N(\text{H I})$  Ly $\alpha$  forest lines are evolving differently than the high  $N(\text{H I})$  Ly $\alpha$  forest lines.

Based on the measurement of  $\tau_{\text{HeII}} = 1.0$  at  $z = 2.4$  by Davidsen et al., if

the He II optical depth is due entirely to the Ly $\alpha$  forest  $\tau_{\text{HeII}}$  should be 2.4 at  $z = 3.3$ . If this value of  $\tau_{\text{HeII}}$  is found, it would imply that the IGM and the Ly $\alpha$  forest are composed of the same type of objects, a view supported by numerical cosmological simulations (Hernquist et al. 1996). If this value of  $\tau_{\text{HeII}}$  were found it would still be possible for there to be a physically distinguishable IGM, but its redshift evolution would have to be the same as the redshift evolution of the Ly $\alpha$  forest. A widespread ionization of the diffuse gas would affect both the IGM and the forest in the same way, and could produce the sort of redshift evolution seen in the forest. Alternatively, a value of  $\tau_{\text{HeII}} \approx 1.7$  at  $z = 3.3$  (the lower limit found by Jakobsen et al. 1994) would imply that either the low column Ly $\alpha$  forest and/or the IGM are evolving less rapidly than the high column Ly $\alpha$  forest, or that the ionizing spectrum is harder at high  $z$ , reducing  $N(\text{He II})/N(\text{H I})$ . A harder spectrum at high redshift is not expected because the UV opacity increases with redshift. Songaila & Cowie (1996) noticed that SiIV/C IV decreases rapidly at redshifts above 3.1, which they account for as due to a softening of the ionizing spectrum due to the IGM becoming optically thin to He I ionizing photons; additional data from Boksenberg (private communication), however, does not support this trend.

## 5. Line Clustering

To investigate any possible clustering of the forest lines we calculated the two point correlation

$$\xi(v) = \frac{N(v)}{N_{exp}(v)} - 1, \quad (7)$$

where  $N(v)$  is the number of line pairs with velocity separation  $v$  in the line list, and  $N_{exp}(v)$  is the number of line pairs expected if the lines were randomly placed along the line of sight.  $N_{exp}(v)$  and the  $1 \sigma$  error bars were calculated via Monte Carlo simulations. For each echelle order in the real spectrum, the number of lines found in that order were randomly placed in the redshift range covered by the order.  $N_{exp}(v)$  was then calculated from the line list containing the randomly placed lines from all orders. The process was repeated 2,500 times to get an average value for  $N_{exp}(v)$  and a reliable standard deviation. We randomly placed lines within each echelle order as opposed to the entire spectrum because we are primarily interested in clustering on small velocity scales, and we wanted to avoid any effects that may be caused by the fact that the higher SNR orders generally have more lines than the lower SNR orders. One order covers a velocity range of  $\approx 4000 \text{ km s}^{-1}$ .

The  $\xi(v)$  function for all 466 Ly $\alpha$  forest lines in our spectrum is presented in Figure 15. The drop below  $50 \text{ km s}^{-1}$  indicates that our spectrum is missing 106 line pairs below  $50 \text{ km s}^{-1}$ . Since the easiest ways to lose a line pair at low velocity separations is to have one line blanket another or to have two lines blend into one line, we believe that we are missing approximately 106 lines from our line list due to blending and blanketing (assuming that there is no intrinsic clustering). The missing lines will have parameters distributed like the observed distributions, so the most likely  $N(\text{H I})$  of a missing line is about  $10^{12.5} \text{ cm}^{-2}$  (Figure 3), and the most likely  $b$  value is about  $23 \text{ km s}^{-1}$  (Figure 4). The lines that were blanketed will have been dropped from the line list, but some lines that are missing because of blending will have significantly altered the  $b$  value of the line that was observed. There should be negligible blending of lines that are separated by more than  $50 \text{ km s}^{-1}$  because the  $\xi(v)$  does not show any deficit of lines at those separations. Because the components of blends had  $N(\text{H I}) \approx 10^{12.5}$  and a  $b \approx 23 \text{ km s}^{-1}$ , the blended lines should have  $N(\text{H I}) > 10^{12.5}$  and  $b$  values of at most  $50 + 23 \text{ km s}^{-1} \approx 70 \text{ km s}^{-1}$ . The 106 missing lines are hence capable of producing much of the “hump” in the observed  $N(\text{H I})$ - $b$  distribution (Figure 5). However, because it would be difficult for these blended lines to produce a line with  $b > 70 \text{ km s}^{-1}$ , it seems unlikely that the tail of the observed  $b$  distribution above  $70 \text{ km s}^{-1}$  can be accounted for by blending. This lends credence to our suspicions that the extended non-Gaussian tail above  $b = 80 \text{ km s}^{-1}$  in the observed distribution is real or a result of continuum placement errors in the real data.

We see no evidence for significant clustering on any scale. Over the velocity range  $50 < v < 150 \text{ km s}^{-1}$  we find  $\langle \xi \rangle = 0.06 \pm 0.045$ , which is 5.8 standard deviations from the value of  $0.32 \pm 0.08$  found by Webb (1987), and 2.4 standard deviations from the value of  $0.17 \pm 0.045$  found by Hu et al. (1995) over the same velocity range.

The lack of clustering in the entire line sample might be because our line list contains considerably more lines at lower column densities than the other studies, and it is suspected that lines with higher  $N(\text{H I})$  cluster more strongly (Crofts 1989; Chernomordik 1995; Cristiani et al. 1995). However,  $\xi(v)$  for the 84 Ly $\alpha$  lines with  $10^{13.6} < N(\text{H I}) < 10^{14.5}$  (presented in Figure 16) still does not show significant clustering on any scale  $> 50 \text{ km s}^{-1}$ . Our value of  $\langle \xi \rangle = 0.19 \pm 0.24$  over  $50 < v < 150 \text{ km s}^{-1}$  is significantly less ( $2.3 \sigma$ ) than the value of  $0.73 \pm 0.13$  found by Hu et al. for lines in the same  $N(\text{H I})$  range. These lines do cluster in the  $25$ - $50 \text{ km s}^{-1}$  bin, and our value of  $\langle \xi \rangle$  over  $25 < v < 150 \text{ km s}^{-1}$  (same range as before, but now including the  $25$ - $50 \text{ km s}^{-1}$  bin) is

$0.57 \pm 0.21$ . Neither Rauch et al. (1992) or Lu et al. (1996) found clustering on any scale in the Ly $\alpha$  forest. We do not understand why some Ly $\alpha$  forest studies found strong clustering while others do not.

## 6. The Dispersion of the $b$ distribution

Ly $\alpha$  lines have different intrinsic  $b$  values because their temperatures differ or their turbulent velocities differ. Clustering on small velocity scales will also change  $b$  values. If all of the H I  $b$  values measured in Ly $\alpha$  forest clouds are thermal, simple photoionization models in which the clouds are in thermal equilibrium and heated only by the UV background flux predict that the baryonic content of the Ly $\alpha$  forest would far exceed the total baryonic content of the universe (Press and Rybiki 1993), because the lines with the largest  $b$  values would be very highly ionized and hence must be very massive to account for their observed H I. Hence, the gas is turbulent. If the gas is heated by a means other than the UV background, the H I/H II ratio will generally be lower than for gas heated by photoionization, exacerbating the problem. Spectra of the metal lines associated with moderate column ( $N(\text{H I}) \approx 10^{13}$  to  $10^{14}$  cm $^{-2}$ ) Ly $\alpha$  clouds (SNR  $\approx 100$ ) may be able to measure the turbulent velocities of the clouds, but the issue is currently unresolved.

Several authors (Hu et al. 1995, de la Fuente et al. 1996) have suggested that most of the Ly $\alpha$  forest is at the same temperature, and the entire dispersion observed in the  $b$  distribution is due to strong clustering on velocity scales of 10 km s $^{-1}$ . We call this scenario the isothermal hypothesis. If it is correct, then most of the lines in our line list are blends, and higher SNR observations will resolve some of the blends. This will have several results on the observed distributions. The  $\xi(v)$  function will increase on small velocity scales – it may not rise above unity, but it will increase relative to its present value. The observed  $b$  distribution will become narrower, and the peak of the  $b$  distribution may move to a smaller  $b$ . With this in mind, some credence may be lent to the isothermal hypothesis by the fact that the peak of our  $b$  distribution is 5 km s $^{-1}$  less than that found by Hu et al. (1995), a study similar to ours but with 0.5 to 0.75 the SNR of our data. On the other hand, we find a greater dispersion in the observed  $b$  distribution than Hu et al. (1995), which is inconsistent with the clustering hypothesis.

The lack of observed clustering below 50 km s $^{-1}$  in the full line list is not necessarily inconsistent with the hypothesis. Blending of close lines could wipe out any clustering signature, such that the only clustering signature would be

the shape of the  $b$  distribution. Because it is unclear exactly how the fitting process will treat a clustered intrinsic distribution, simulated-observations will be required to determine the effect of small scale clustering on the observed two point correlation function. Because of the time involved, we have not performed any simulated-observations in which the Ly $\alpha$  clouds are clustered on small velocity scales.

## 7. Redshift Evolution of the Intrinsic Distributions

There are two other studies that have determined the intrinsic distributions of the Ly $\alpha$  forest using the same type of analysis that we have used. Hu et al. (1995) found the intrinsic distributions at  $\langle z \rangle = 2.8$ , and Lu et al. (1996) determined the intrinsic distributions at  $\langle z \rangle = 3.7$ . The SNR of both studies were less than that of our observations, 50 for Hu et al. (1995) and 20-80 for Lu et al. (1996).

We have found (at  $\langle z \rangle = 2.7$ ) the N(H I) and  $b$  distributions, as well as the clustering properties of the clouds, to be nearly identical to that found by Lu et al. (1996) at  $\langle z \rangle = 3.7$ . However, as previously noted, we found a different  $b$  distribution and different clustering properties than Hu et al. (1995), which was done at the same redshift as our study. Although we do not understand why Hu et al. (1995) found different cloud properties than we did, we suspect that the differences in the derived intrinsic distributions stem from different procedures used to fit the absorption lines, because we both used simulated-observations to remove SNR effects from the data.

Both Lu et al. (1996) and ourselves used the VPFIT software to fit absorption lines, and we both used simulated-observations to determine the intrinsic distributions of the Ly $\alpha$  forest. Because of this we believe that a meaningful comparison can be made between our results, and we conclude that there is almost no redshift evolution of the Ly $\alpha$  forest (other than in the number of absorbers). The only apparent difference is in the dispersion of the  $b$  distribution, which we found to be  $14 \text{ km s}^{-1}$  whereas Lu et al. (1996) found it to be  $8 \text{ km s}^{-1}$ . Although we have not done the simulations to measure the error on our value of  $14 \text{ km s}^{-1}$ , but we believe the error may be as large as 3 or  $4 \text{ km s}^{-1}$  – and that the difference between our value and that reported by Lu et al. (1996) is not necessarily significant.

We thank the referee, L. Lu, for many helpful comments. We thank J. Aycock and J. Killian at the W.M. Keck Observatory for help during the

observations. D. Welty found metal identifications for several of the narrow lines in the spectra. We thank T. Barlow for providing a copy of his code that automatically extracts and wavelength calibrates HIRES data. We thank R. Carswell for providing a copy of his Voigt profile fitter, VPFIT. We thank S. Rappoport for aid with the simulations. We thank P. Petitjean, and M. Rauch and especially S. Burles for very helpful discussions. This work was supported in part by grants AST-9420443 and NAGW-4497.

## REFERENCES

- Cen R., and Ostriker, J.P. 1993, *ApJ*, 417, 404
- Carswell R.F., Lanzetta K.M., Parnell H.C., & Webb J.K. 1991, *ApJ*, 371, 36
- Carswell, R.F., Morton, D.C., Smith, M.G., Stockton, A.N., Turnshek, D.A., & Weymann, R.J. 1984, *ApJ*, 278, 486
- Chernomordik, V. V. 1995, *ApJ*, 440, 431
- Cowie, L.L., Songaila, A., Kim, T.-S. & Hu, E.M. 1995, *AJ*, 109, 1522
- Cristiani, S., D’Odorico, S., Fontana, A., Giallongo, E., & Savaglio, S., *MNRAS*, 273, 1016
- Crotts, A.P.S. 1989, *ApJ*, 336, 550
- de la Fuente A., Rodriguez Pascual P.M., Sanz J.L., Recondo M.C. 1996, *MNRAS*, 281, 463
- Dinshaw, N., Foltz, C.B., Impey, C.D., Weymann, R.J., & Morris, S.L. 1995, *Nature*, 373, 223
- Duncan, R.C., Vishniac, E.T., & Ostriker, J.P. 1991, *ApJ*, L1
- Fan X., and Tytler D., 1994, *ApJS*, 94, 17
- Giallongo, E., and Petitjean, P. 1994, *ApJ*, 426, L61
- Hagen, H.-J., Cordis, L., Engels, D., Groote, D., Haug, U., Heber, U., Koehler, Th., Wisotzki, L., & Reimers, D. 1992, *A&A*, 253, L5
- Hernquist, L., Katz, N., Weinberg, D.H., & Miralda-Escude, J. 1996, *ApJ*, 457, L51
- Hu, E., Kim, T.-S., Cowie, L. L., Songaila, A., & Rauch, M. 1995, *AJ*, 110, 1526
- Jackobsen, P., Boksenberg, A., Deharveng, J. M., Greenfield, P., Jedrzejewski, R., & Paresce, F. 1994, *Nature*, 370, 35

- Lanzetta, K.M., Bowen, D.V., Tytler, D., & Webb, J.K. 1995, *ApJ*, 442, 538
- Lanzetta, K.M., Wolfe, A.M., Turnshek, D.A., Lu, L., McMahon, R.G., & Hazard, C. 1991, *ApJS*, 77, 1
- Lu L., Savage B.D., Tripp T.M., & Meyer D.M. 1995, *ApJ*, 447, 597
- Lu L., Sargent W.L.W., Womble D.S., & Takada-Hidai M. 1996, *ApJ*, 472, 509
- Meiksin A., & Madau P. 1993, *ApJ*, 412, 34
- Melott, A.L. 1980, *ApJ*, 241, 889
- Miralda-Escude J., and Rees, M. 1993, *MNRAS*, 260, 617
- Miralda-Escude, J., 1993, *MNRAS*, 262, 273
- Petijean, P., Bergeron, J., Carswell, R.F., & Puget, J.L. 1993, *A&A*, 260, 67
- Petitjean, P., Webb, J.K., Rauch, M., Carswell, R.F., & Lanzetta, K. 1993, *MNRAS*, 262, 499
- Pettini M., Hunstead R.W., Smith L.J., & Mar D.P. 1990, *MNRAS*, 246, 545
- Rauch M., Carswell R.F., Chaffee F.H., Foltz C.B., Webb J.K. Weymann R.J., Bechtold J., & Green R.F. 1992, *ApJ*, 390, 387
- Rauch M., Carswell R.F., Webb J.K. & Weymann R.J. 1993, *MNRAS*, 260, 589
- Rauch M., Miralda-Escude J., Sargent W.L.W., Barlow T.A., Weinberg D.H., Hernquist L., Katz N. Submitted to *Apj*
- Sargent, W.L.W., Young, P., Boksenberg, A., & Tytler, D. 1980, *ApJS*, 42, 41
- Smette, A., Surdej, J., Shaver, P.A., Foltz, C.B., Chaffee, F.H., Weymann, R.J., & Magain, P. 1991, *ApJ*, 389, 39
- Songaila, A., Hu, E.M., & Cowie, L.L. 1995, *Nature*, 375, 124
- Songaila, A., & Cowie, L.L. 1996, 112, 335AJ
- Tytler D., Fan X.M., Burles S., Cottrell L., Davis C., Kirkman D., & Zuo L. 1995, "Ionization and Abundance of Intergalactic Gas", in *Proc. ESO Workshop*, eds. Bergeron J., Meylan G., & Wampler J.
- Tytler D. & Burles S. 1996, *Conference Proceeding of the International Symposium on "Origin of Matter and Evolution of Galaxies in the Universe"*, Atami, Japan, January 18-20, 1996.
- Verner D.A., Tytler D., & Barthel P.D. 1994, *ApJ*, 430, 186
- Vogt, S.S., et al. 1994, *Proc. SPIE*, 2198, 362

Webb J. K. 1987, in *Observational Cosmology*, Proc. of IAU Symposium No. 124, edited by A. Hewitt, G. Burbidge, and L. Z. Fang (Reidel, Dordrecht), p. 803

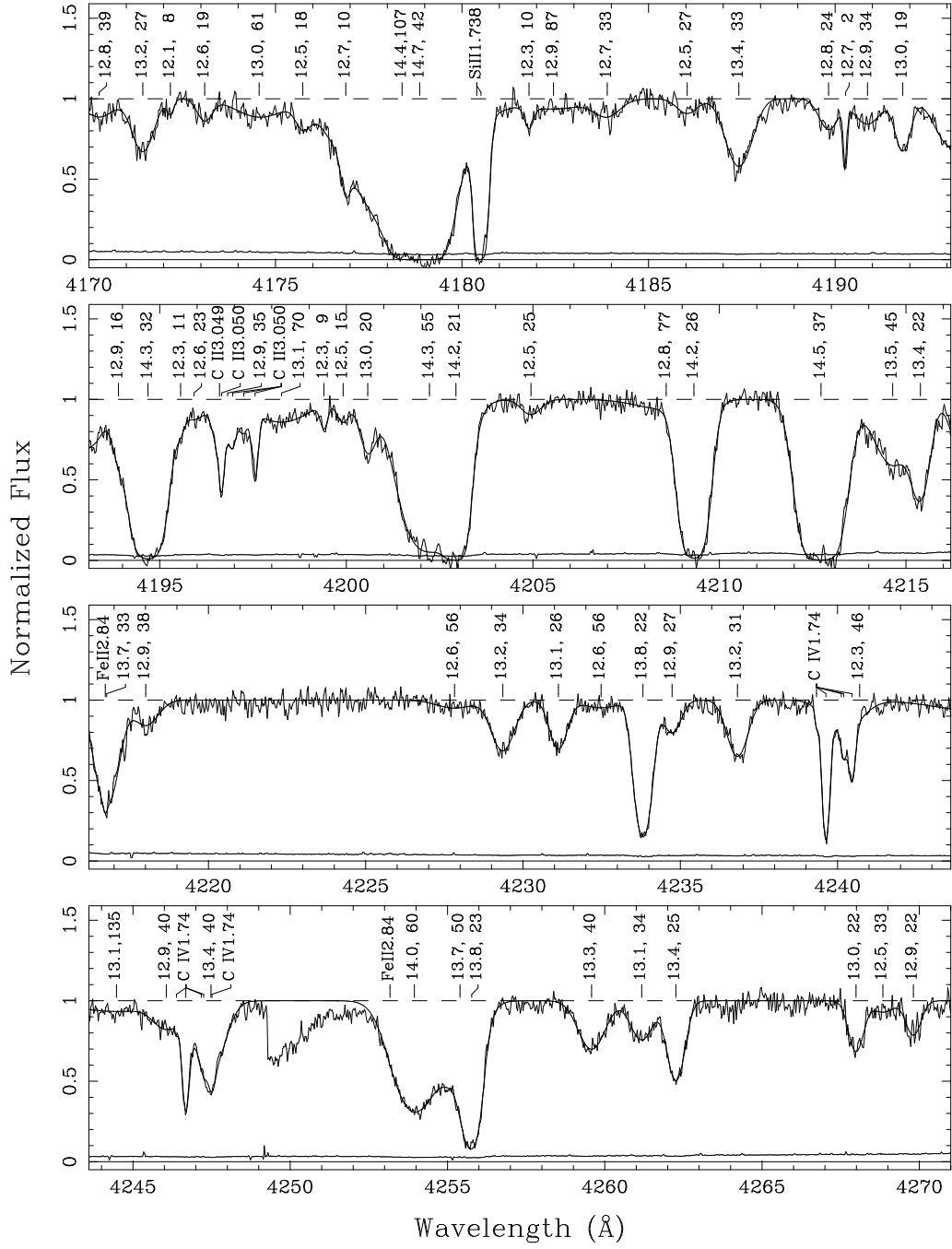
Weinberg D.H., Miralda-Escude J., Hernquist L., & Katz N., Submitted to *ApJ*

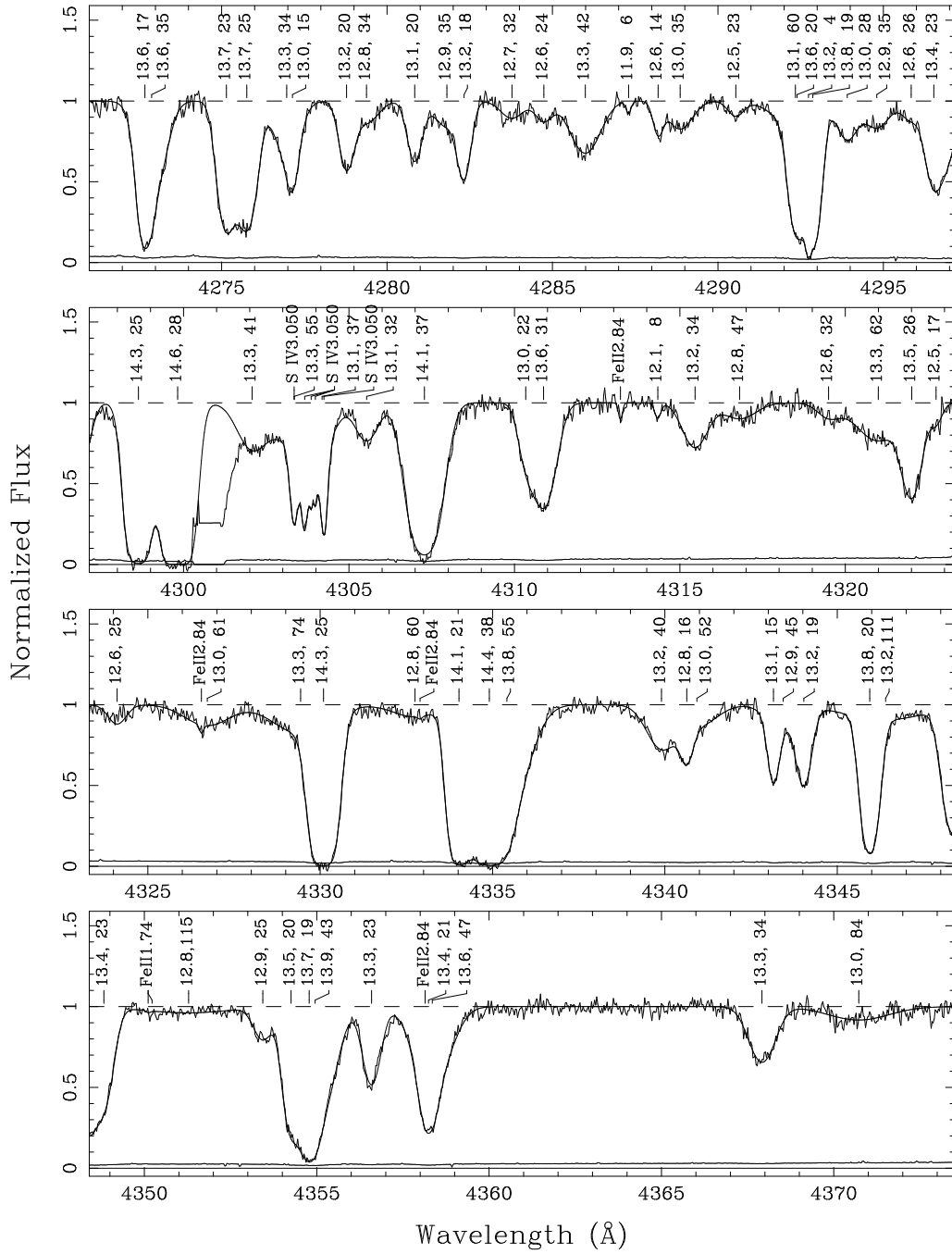
Williger G.M., Baldwin J.A., Carswell R.F., Cooke A.J., Hazard C., Irwin M.J., McMahon R.G., & Storrie-Lombardi L.J. 1994, *ApJ*, 428, 574

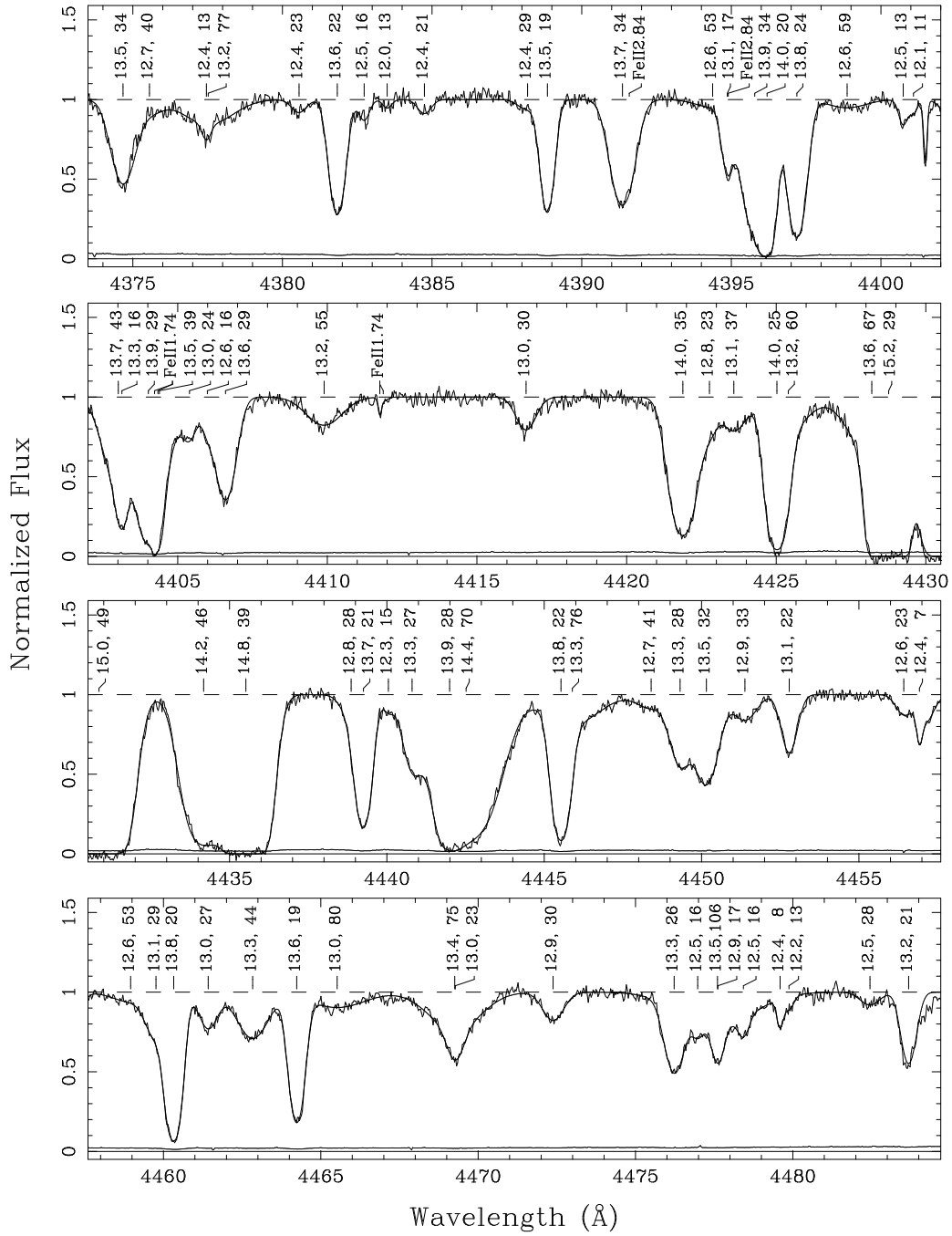
Zhang Y., Anninos P., & Norman M.L. 1995, *ApJ*, 453, L57

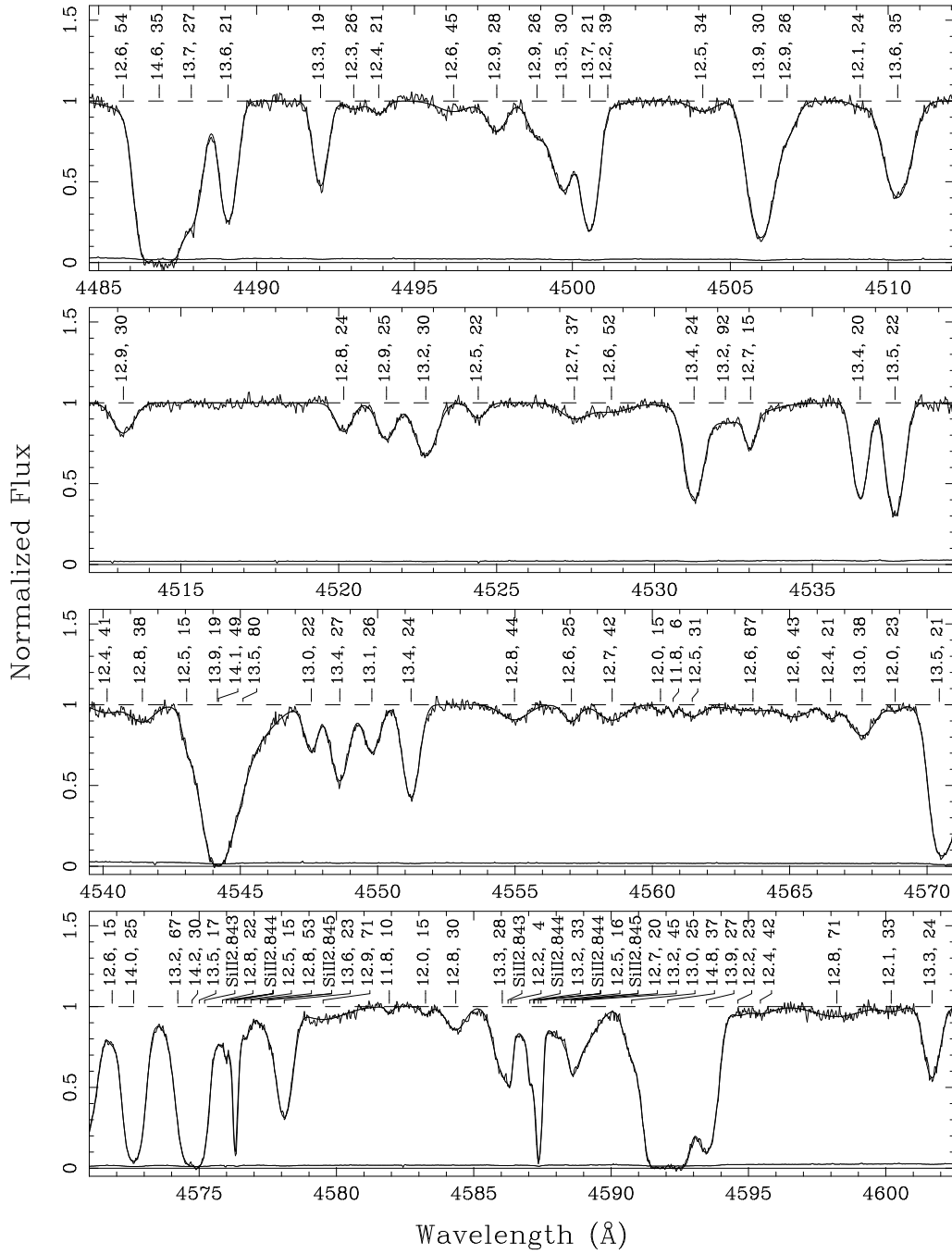


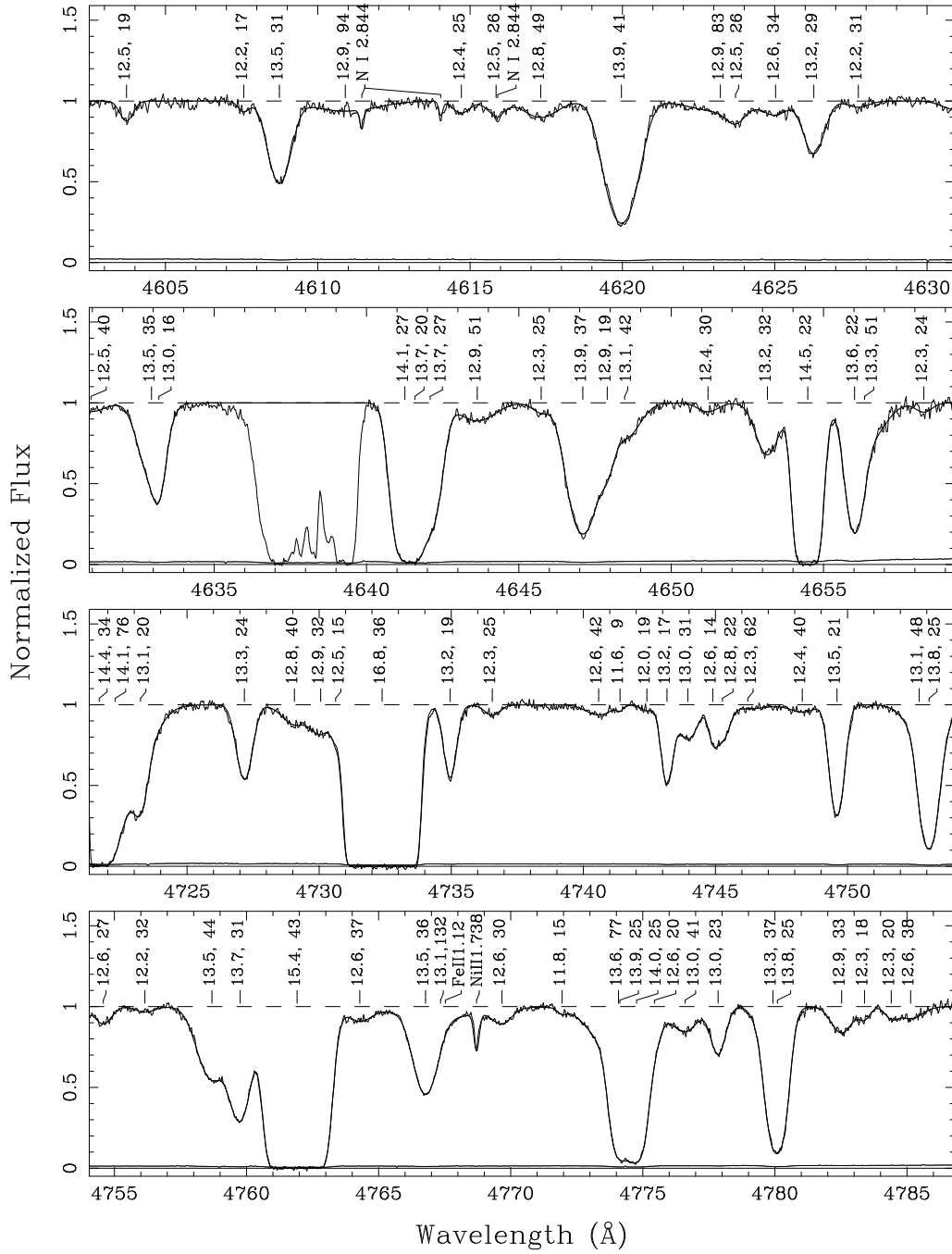
Fig. 1.— The spectrum of QSO HS 1946+7658 . We indicate 466 Ly $\alpha$  forest lines and 73 metal lines. The spectrum is normalized to a continuum level of one. Wavelengths are vacuum heliocentric values. The log column density (in  $\log \text{cm}^{-2}$ ) and velocity dispersion (in  $\text{km s}^{-1}$  ) of each line are displayed above a tick mark indicating the center of the line. Identified metal ions are indicated along with the redshift of the metal system. The calculated  $1\sigma$  error spectrum (per pixel) is shown just above zero on the same scale. The pixels size is  $2 \text{ km s}^{-1}$

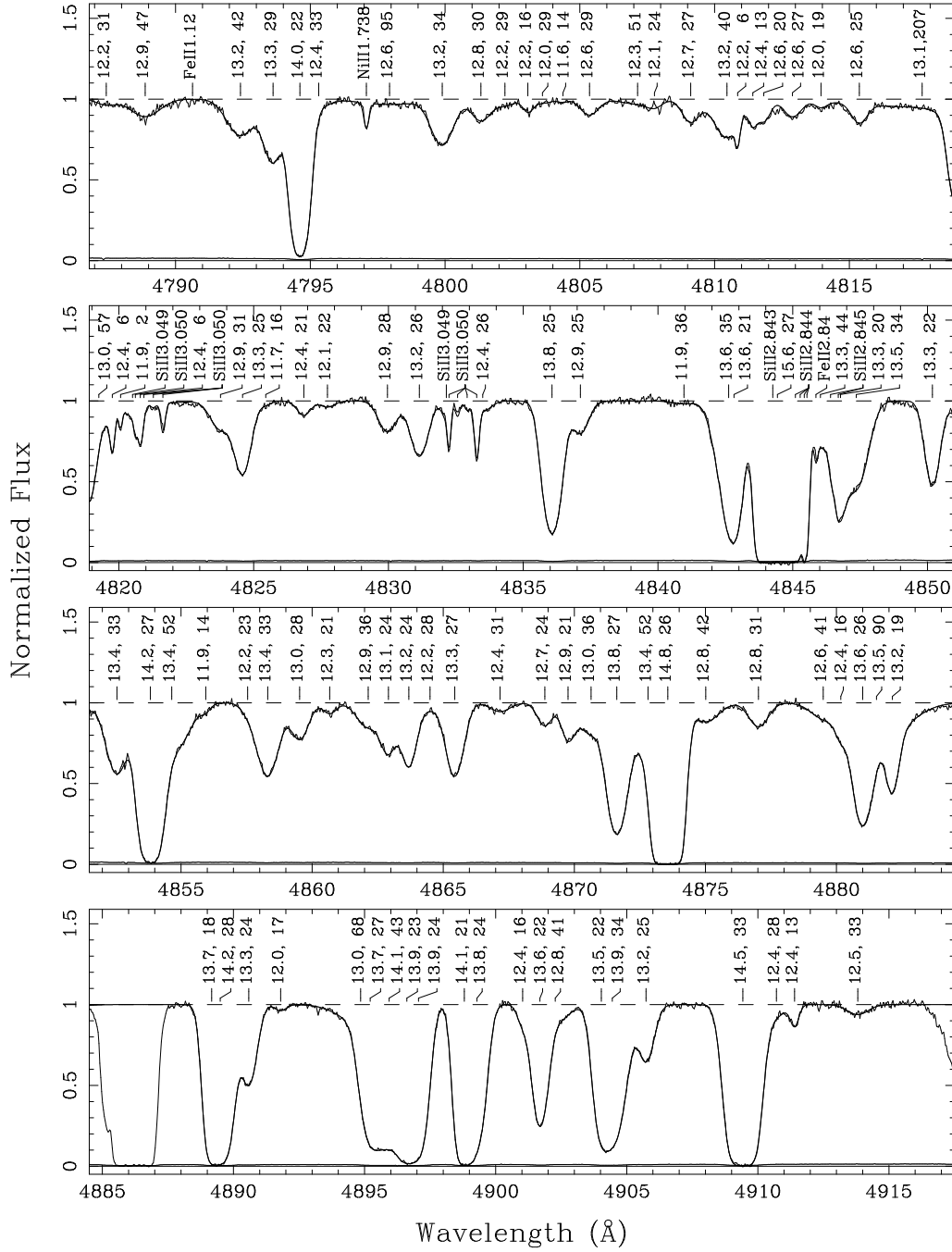












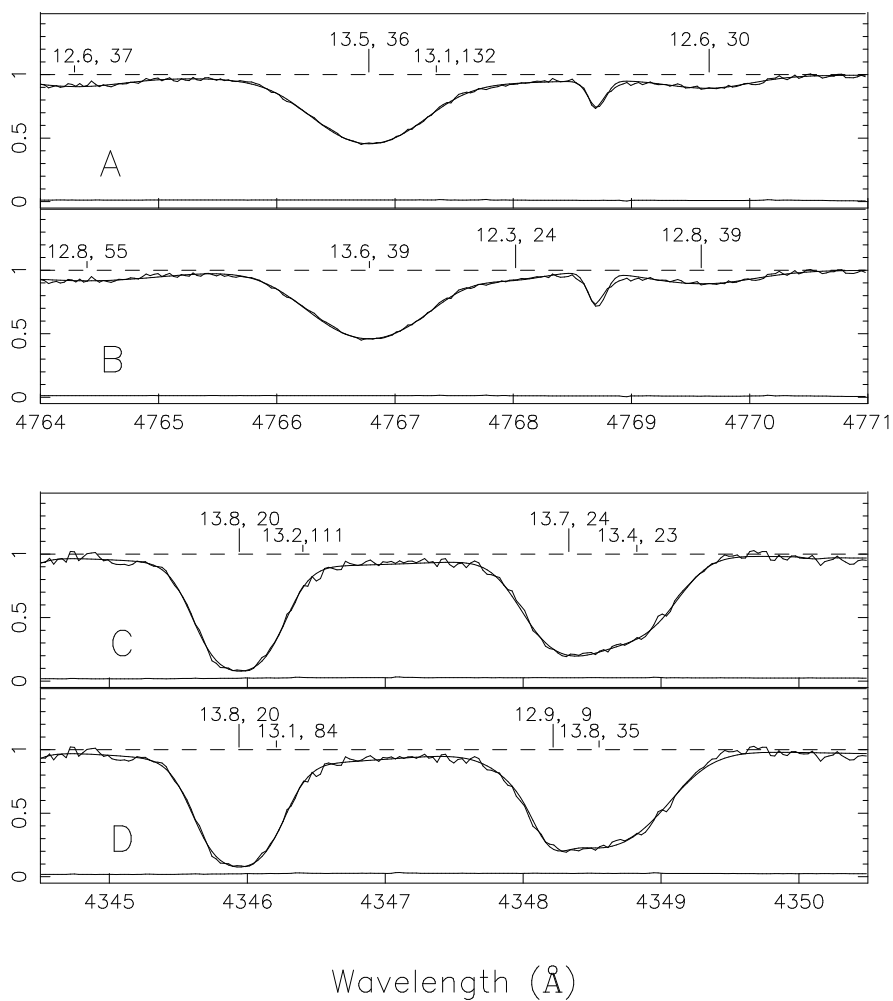


Fig. 2.— Examples of the non-uniqueness of the line fitting process. Panels A and B show the same region of spectra fit by different sets of Voigt profiles; panels C and D show a different region of spectra. The paired fits were started with slightly different parameter, which led to a different local minima. The line near 4768.7 Å is an Fe II ( $z=1.12$ ) line constrained by other transitions, and was not varied during the fitting process. The reduced  $\chi^2$  for each region are as follows: Panel A – 0.83, B – 1.15, C – 1.04, D – 1.16.



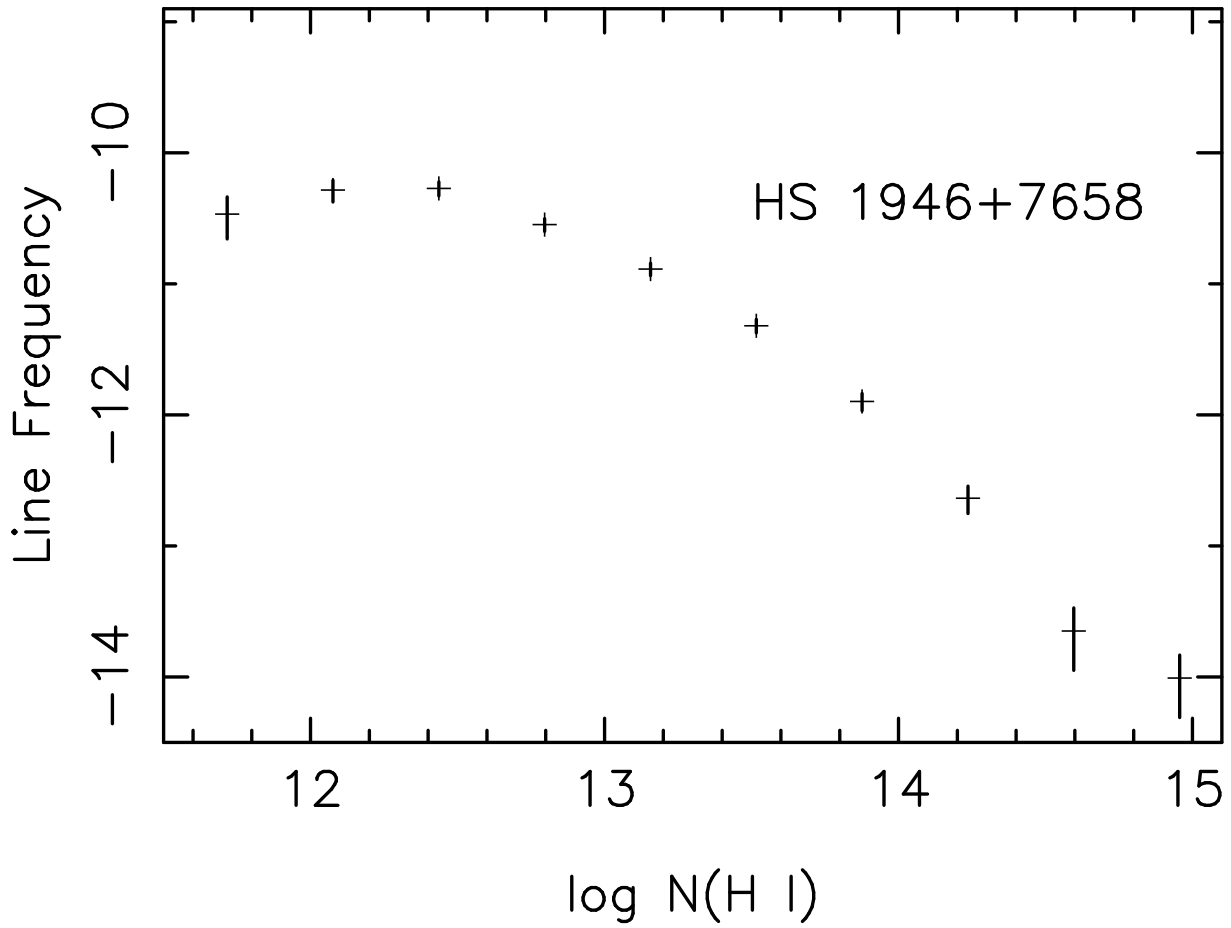


Fig. 3.— The observed  $N(\text{H I})$  distribution towards HS 1946+7658. The lines have been binned into intervals of 0.36 in  $\text{Log } N(\text{H I})$ , starting from 11.75. The vertical bars represent  $1 \sigma$  errors. The first bin has 8 lines.

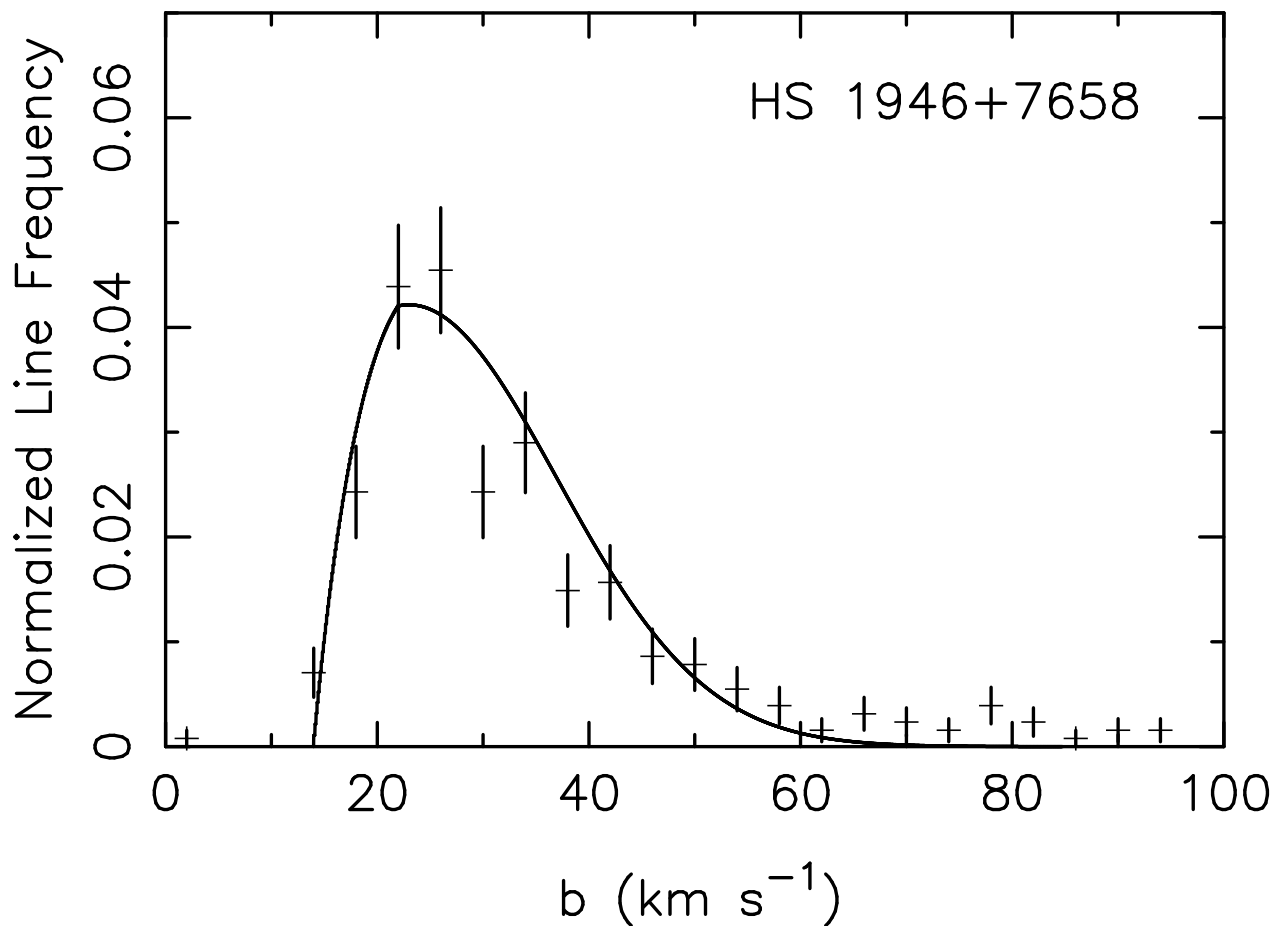


Fig. 4.— The observed  $b$  distribution towards HS 1946+7658. The lines have been binned into intervals of  $4 \text{ km s}^{-1}$  in  $b$ . The vertical bars represent  $1 \sigma$  errors. The curve is our best estimate of the intrinsic  $b$  distribution – a Gaussian with mean  $23 \text{ km s}^{-1}$ ,  $\sigma_b = 14 \text{ km s}^{-1}$ , and  $b_{min}$  given by Equation 4. We believe that most of the lines with  $b < 14 \text{ km s}^{-1}$  are not part of the intrinsic  $b$  distribution. The lines with  $b > 60 \text{ km s}^{-1}$  are probably real, but some must be blends and some may be continuum errors. The sum of all line frequencies is one.

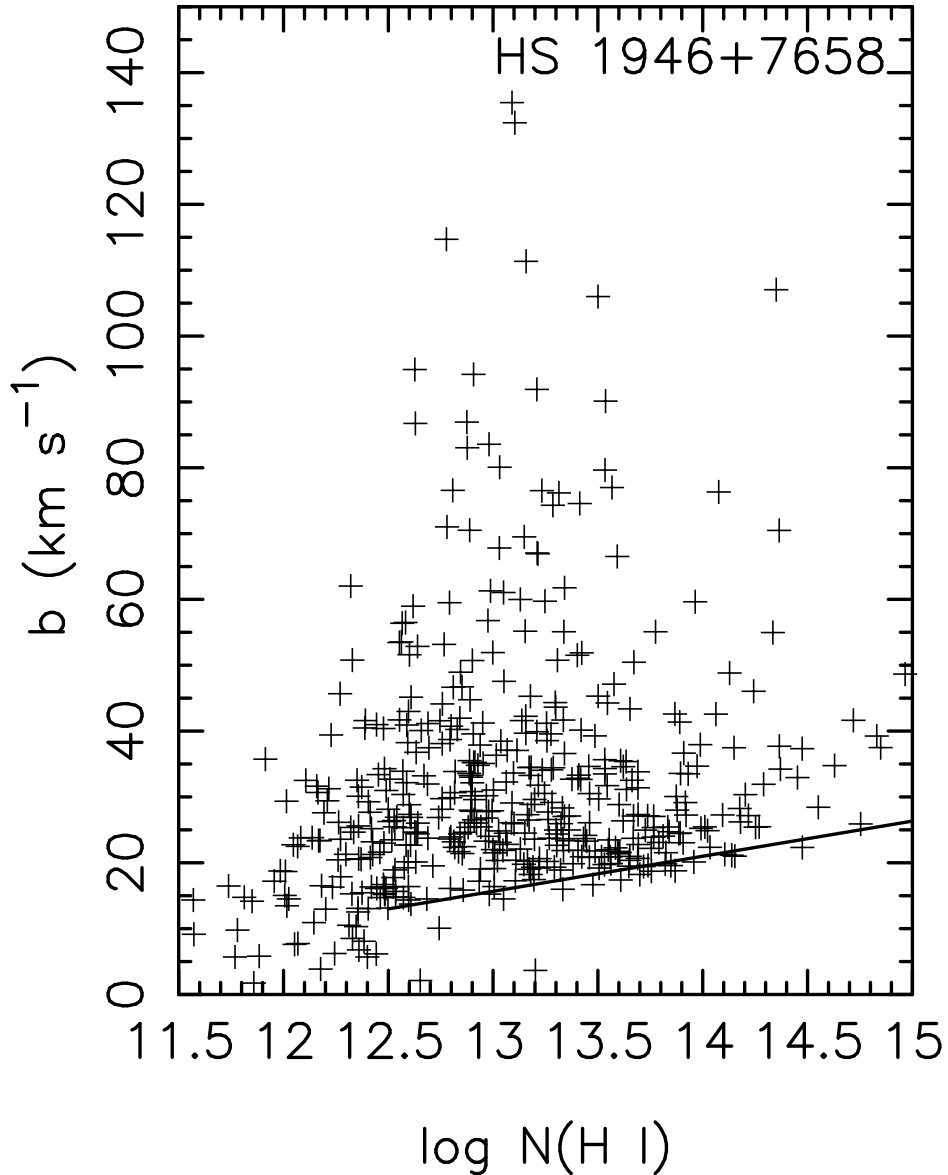


Fig. 5.— The observed  $N(\text{H I})$ - $b$  distribution of  $\text{Ly}\alpha$  lines towards HS 1946+7658. The position of each line is indicated by a cross. Errors have not been displayed. They are listed in Table 1. The solid line is the lower cutoff in the  $b$  distribution described in Section 3.6 (Equation 4). The 3 lines below this cutoff with  $N(\text{H I}) > 10^{12.5}$  are all real. They may be metals (Section 3.7).

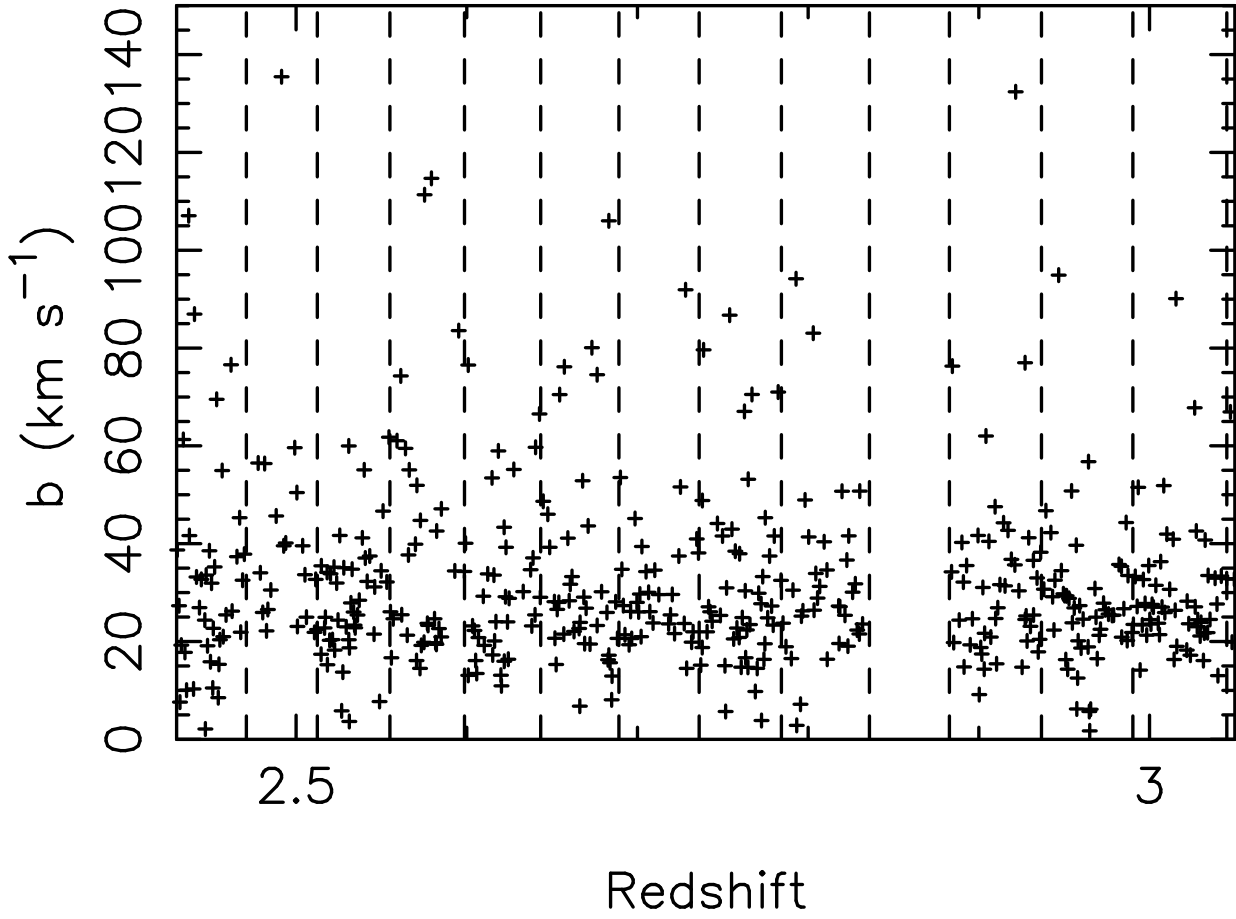


Fig. 6.— The observed  $z$ - $b$  distribution towards HS 1946+7658. The boundaries of the echelle orders are indicated by dashed vertical lines.

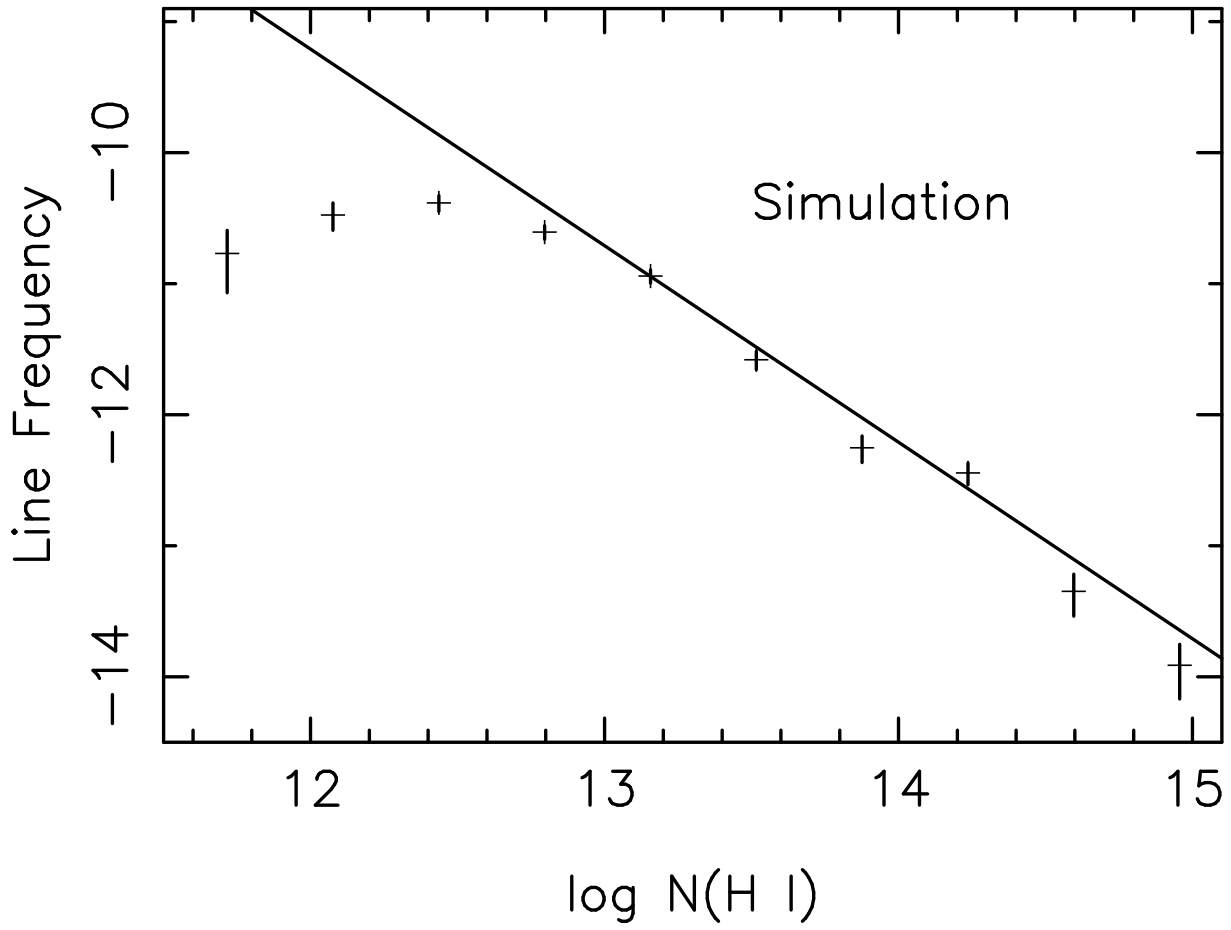


Fig. 7.— Simulated-observations. The intrinsic  $N(\text{H I})$  distribution (straight line, given by Equation 2) and the results of the simulated-observations, binned into intervals of 0.25 in  $\text{Log } N(\text{H I})$ . The vertical bars are  $1 \sigma$  errors in the simulated-observations.

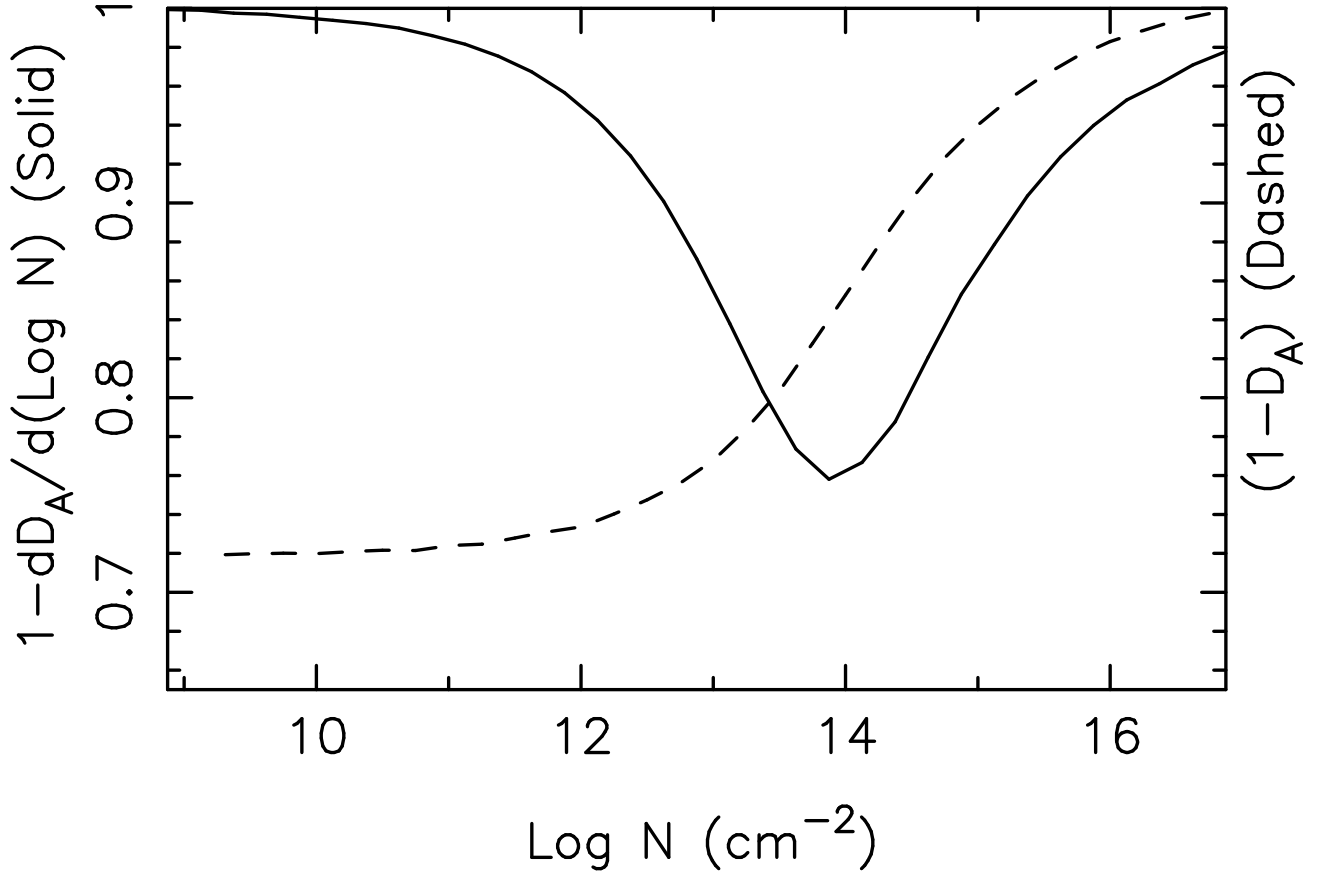


Fig. 8.— The dashed line shows the mean H I Ly $\alpha$  absorption ( $D_A$ ) from an intrinsic population with a N(H I) distribution given by Equation 2 at  $N(\text{H I}) < 10^{17} \text{ cm}^{-2}$  plotted against  $N_{min}$  of the distribution. This ignores continuum absorption. The solid line shows the differential mean H I Ly $\alpha$  absorption of the same population of clouds as a function of N(H I). Note that most of the H I Ly $\alpha$  forest opacity occurs in clouds with  $10^{13} < N(\text{H I}) < 10^{15}$ , and that the differential contribution to the Ly $\alpha$  opacity is a maximum at  $N(\text{H I}) = 10^{14} \text{ cm}^{-2}$ .

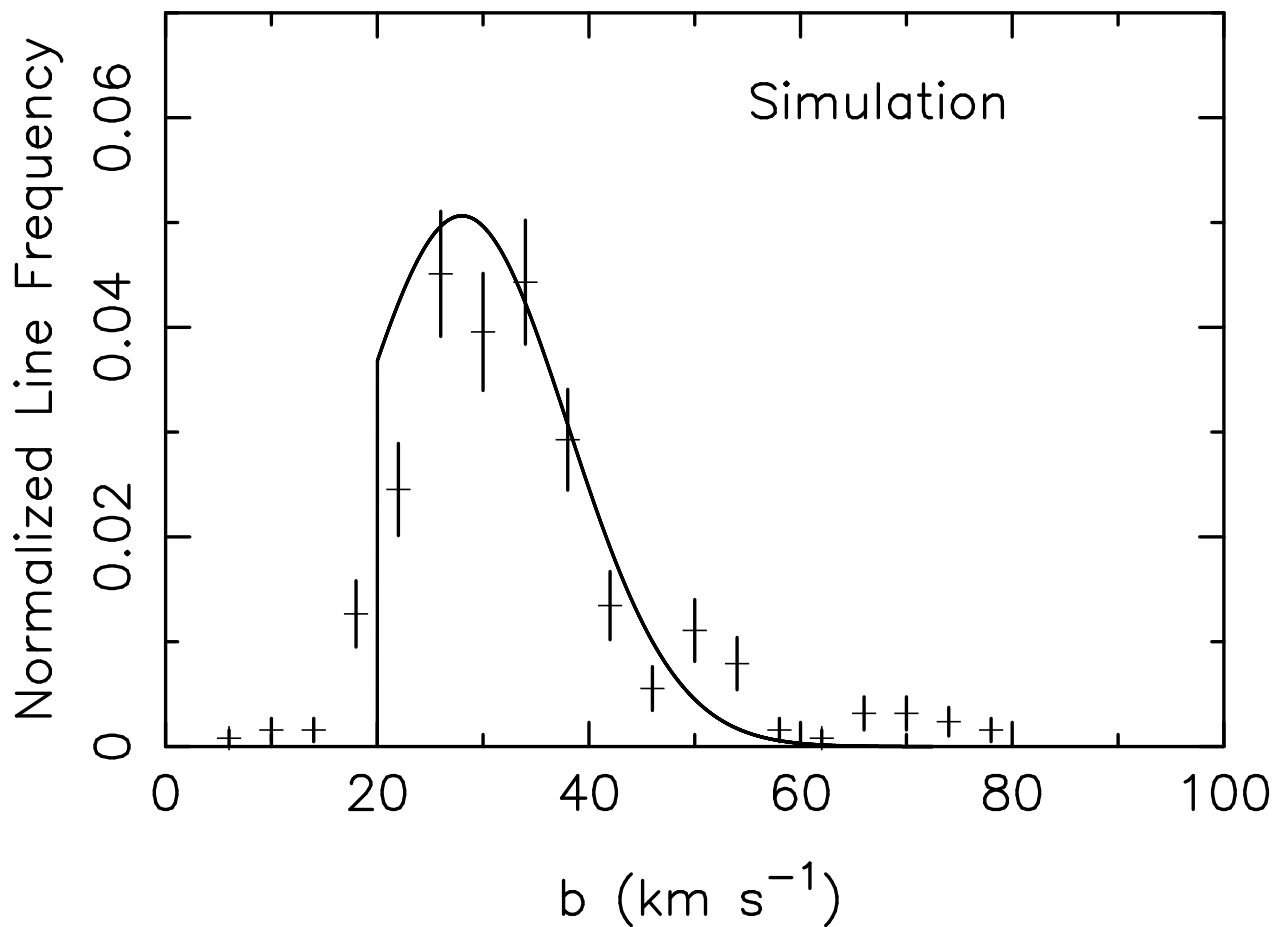


Fig. 9.— The simulated-observation  $b$  distribution and the intrinsic  $b$  distribution for the simulation. The lines were binned into intervals of  $4 \text{ km s}^{-1}$  in  $b$ . The vertical bars are  $1 \sigma$  errors in the simulated-observations. The intrinsic distribution for this simulation (not our best estimate of the true intrinsic distribution) is a truncated Gaussian with mean  $28 \text{ km s}^{-1}$  and  $\sigma_b = 10 \text{ km s}^{-1}$  (displayed as a solid curve). Note that the distribution of output  $b$  values are very similar to the input.

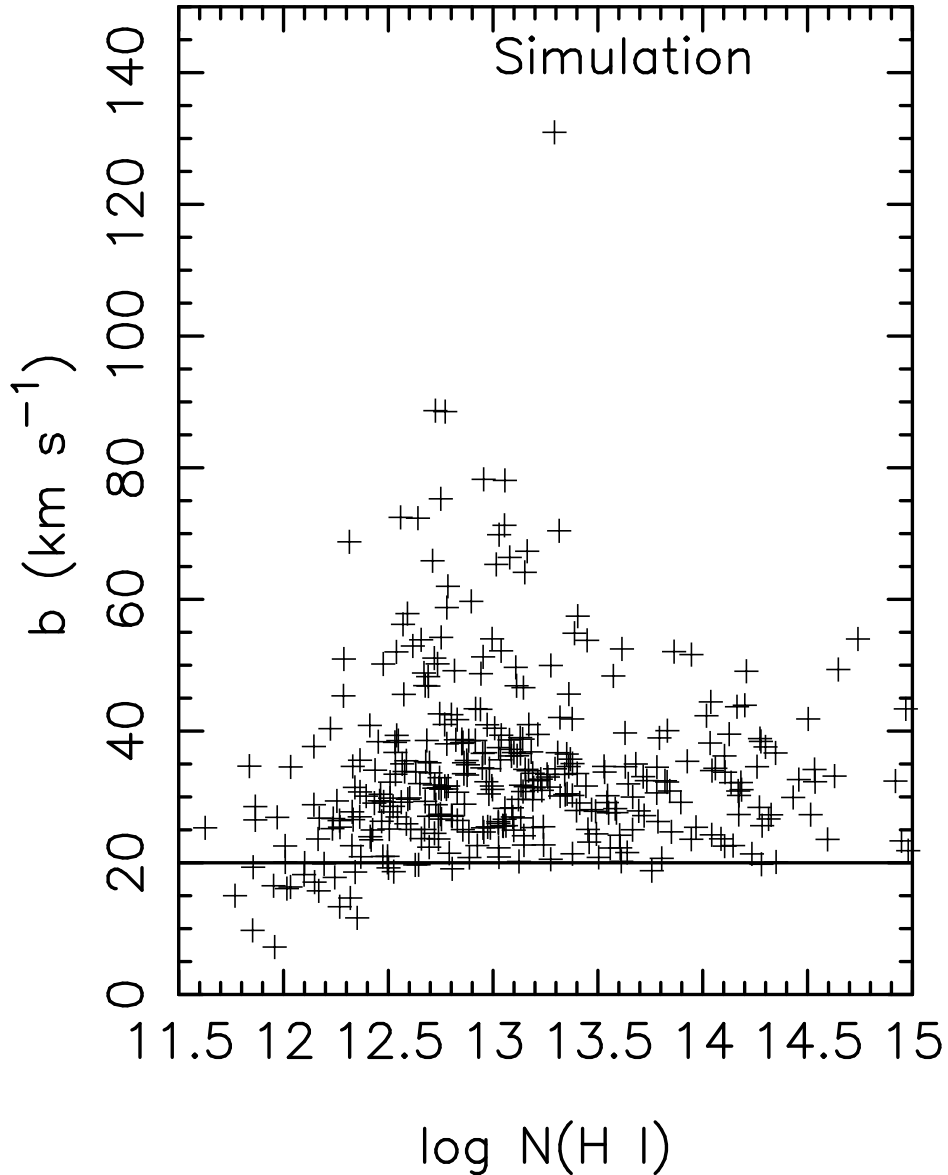


Fig. 10.— The simulated-observation  $N(\text{H I})$ - $b$  distribution. The lines of the simulated-observation are indicated by crosses. The horizontal line at  $20 \text{ km s}^{-1}$  was the lower cutoff in the intrinsic distribution used to create the simulated observation. Note that this lower cutoff is completely preserved for lines with  $N(\text{H I}) > 10^{12.5} \text{ cm}^{-2}$ , but that noise features with  $b < 20 \text{ km s}^{-1}$  appear as spurious lines at  $N(\text{H I}) < 10^{12.5}$ .



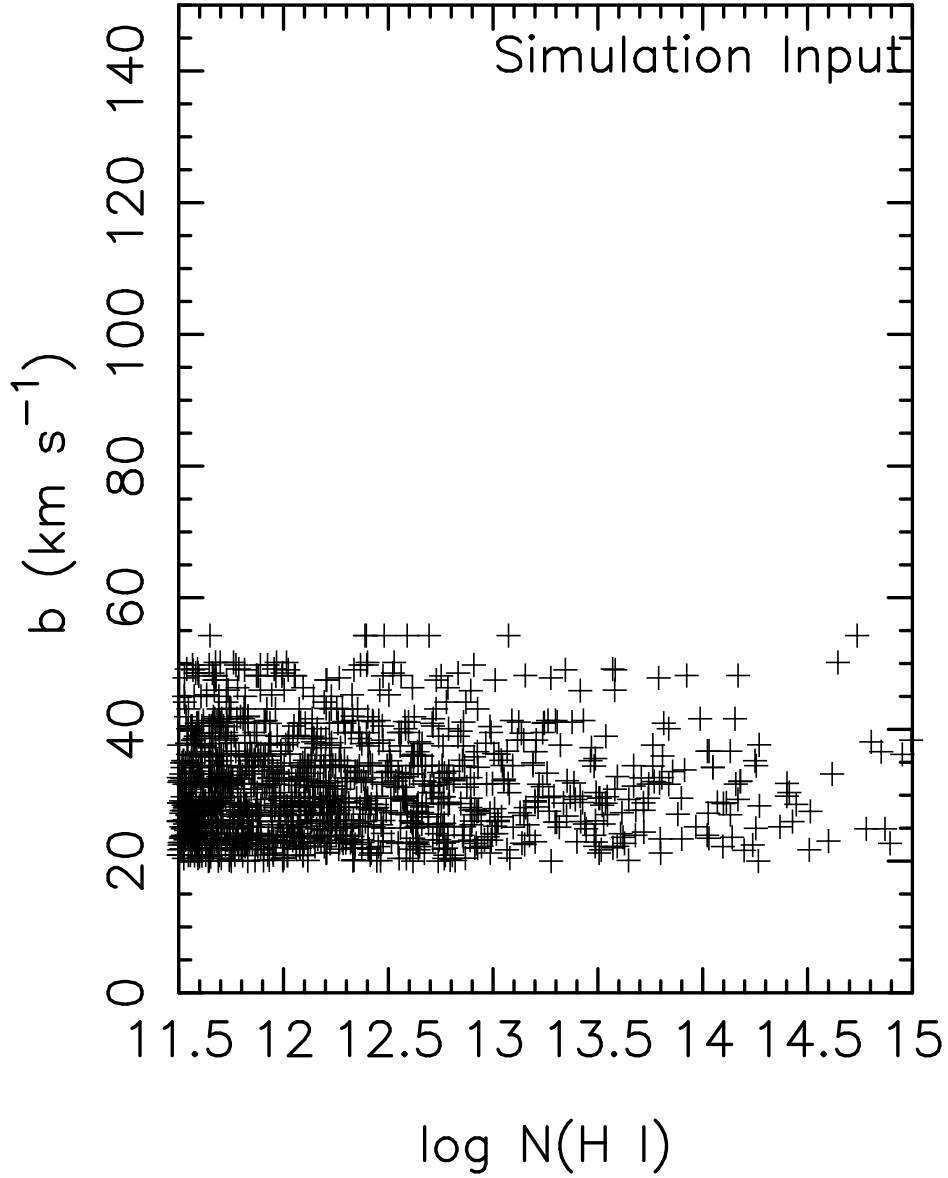


Fig. 11.— The intrinsic  $N(\text{H I})$ - $b$  distribution used to create the data set the simulated-observations were made from. Note the sharp lower cutoff of  $20 \text{ km s}^{-1}$  in the  $b$  distribution.

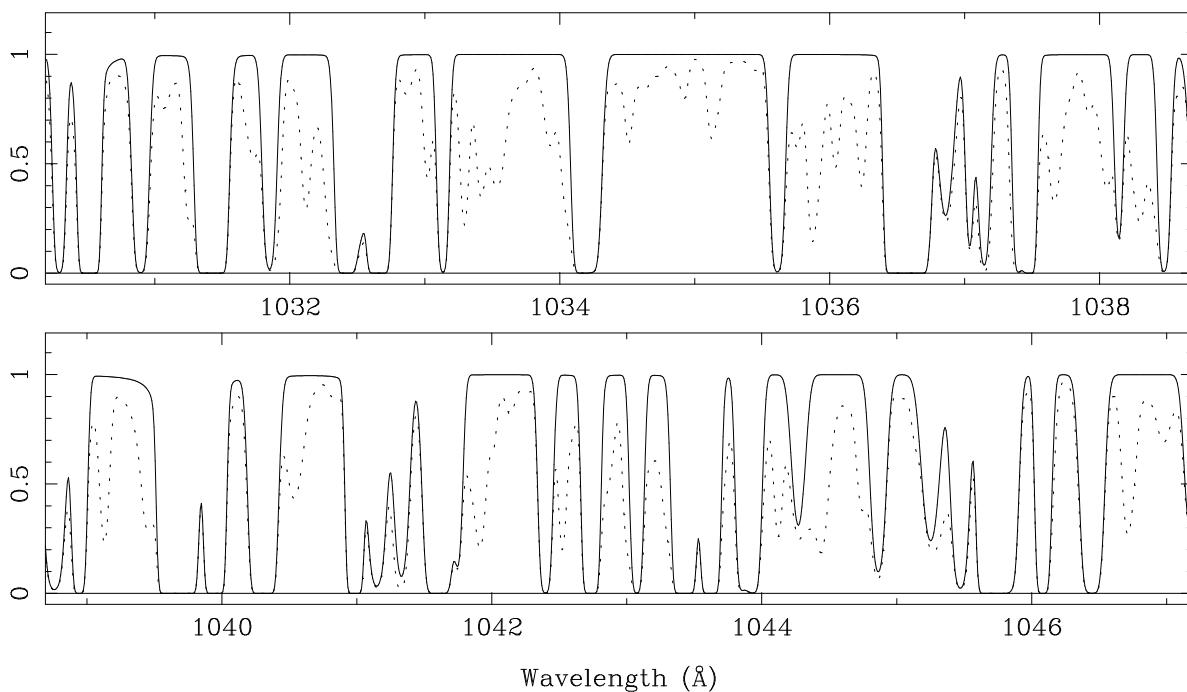


Fig. 12.— A section of simulated  $7.9 \text{ km s}^{-1}$  He II Ly $\alpha$  forest spectra at  $z = 2.4$ . This spectra was created using the H I Ly $\alpha$  forest line distributions, with  $N(\text{He II})/N(\text{H I}) = 100$ . The H I  $b$  values were taken to be thermal. The solid line shows the spectra of Ly $\alpha$  forest clouds with  $N(\text{H I}) > 10^{12.1}$ , the dotted line shows the spectra of all lines with  $N(\text{H I}) > 10^{9.0}$  (effectively zero). No noise has been added to the spectrum. Note that even the spectra with all lines with  $N(\text{H I}) > 9.0$  contains regions with very little absorption.

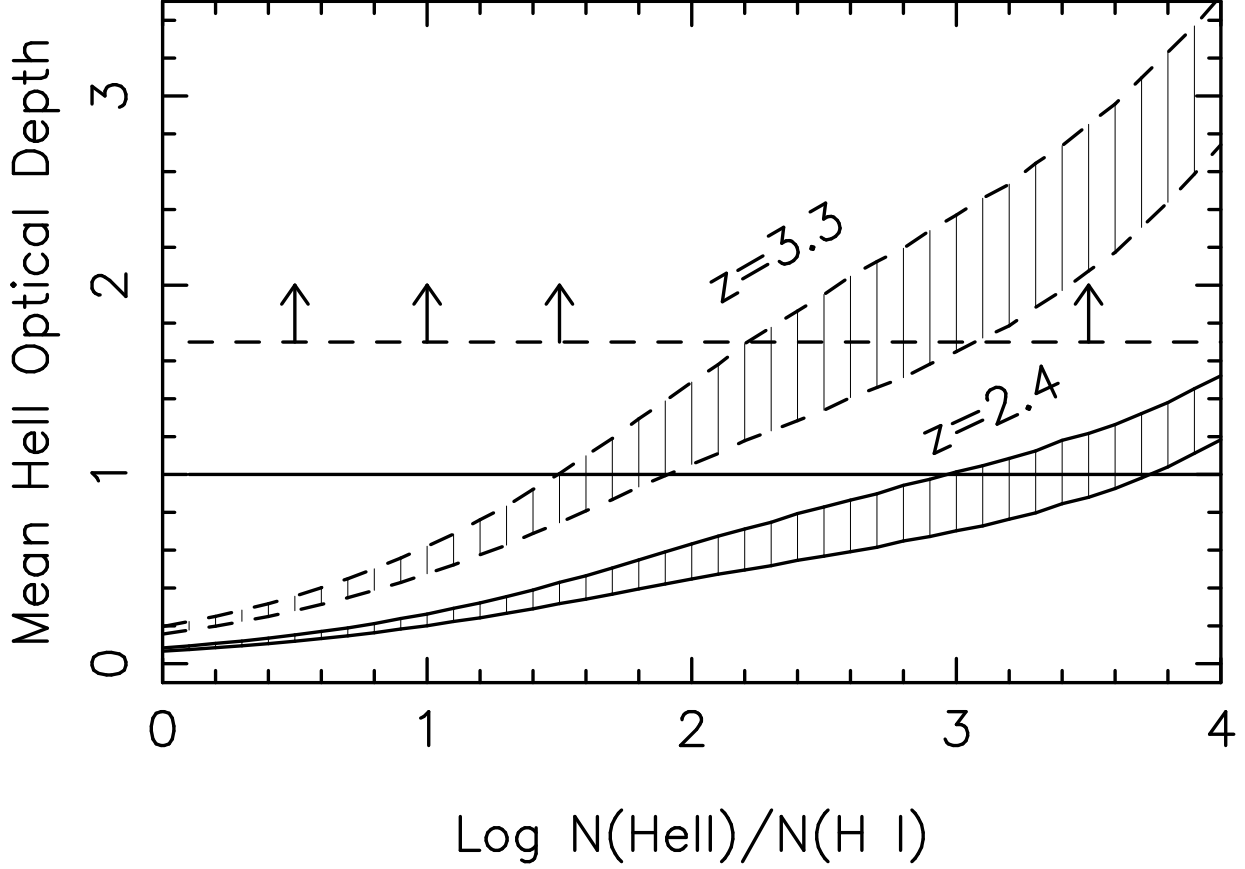


Fig. 13.— Mean He II Ly $\alpha$  forest optical depth with  $N_{\min} = 10^{12.1}$  at  $z = 3.3$  (dashed) and  $z = 2.4$  (solid). The lower curve for each redshift was calculated assuming the H I  $b$  values are entirely thermal, and the upper curve was calculated assuming mostly turbulent  $b$  values (see Section 4 for details). The horizontal lines indicate observed He II optical depths. (1.0 at  $z = 2.4$ , and a lower limit of 1.7 at  $z = 3.3$ ) Note that if the He II optical depth is due entirely to the Ly $\alpha$  forest,  $\tau_{\text{HeII}}$  must be 2.4 at  $z = 3.3$ , if  $N(\text{He II})/N(\text{H I})$  is constant with  $z$ .

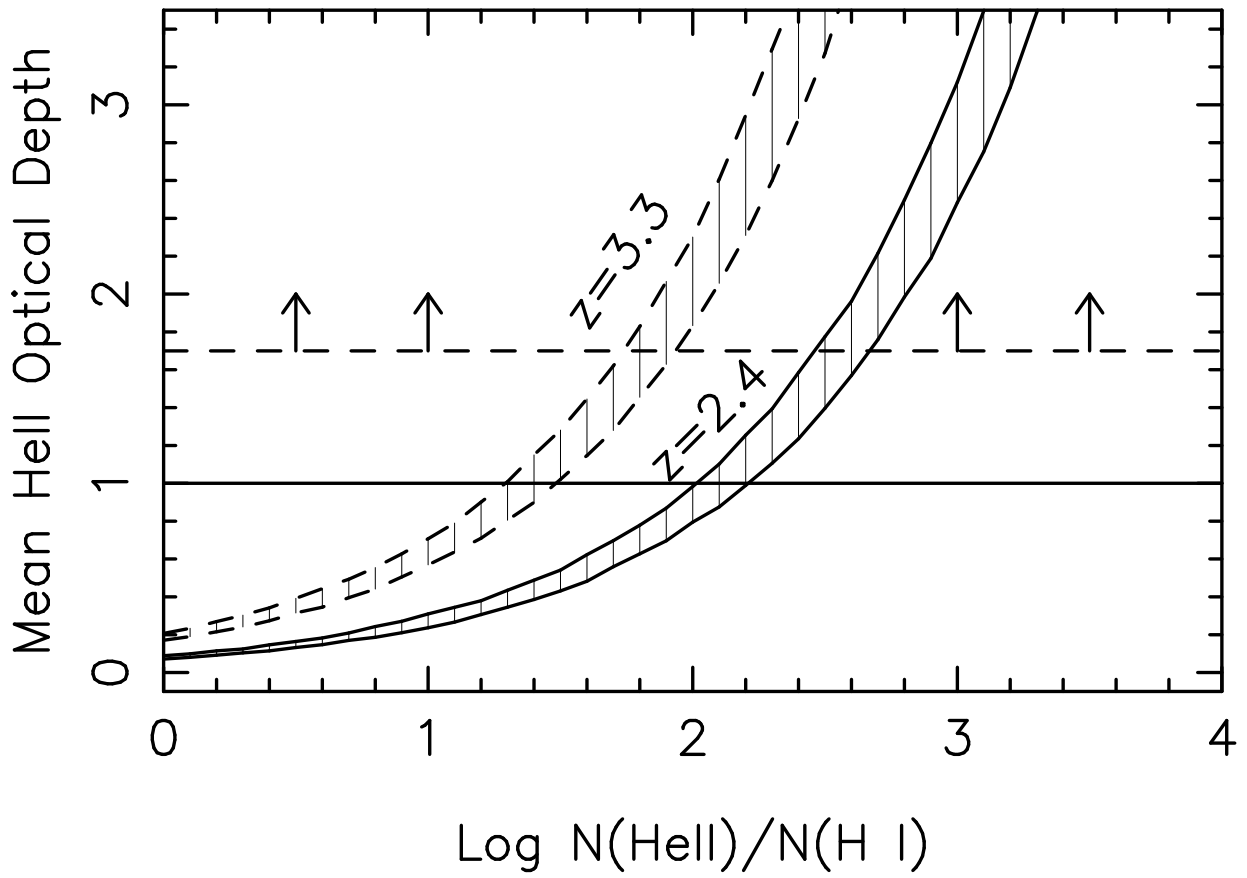


Fig. 14.— Same as Figure 11 but with  $N_{\min} = 10^{9.0} \text{ cm}^{-2}$ .

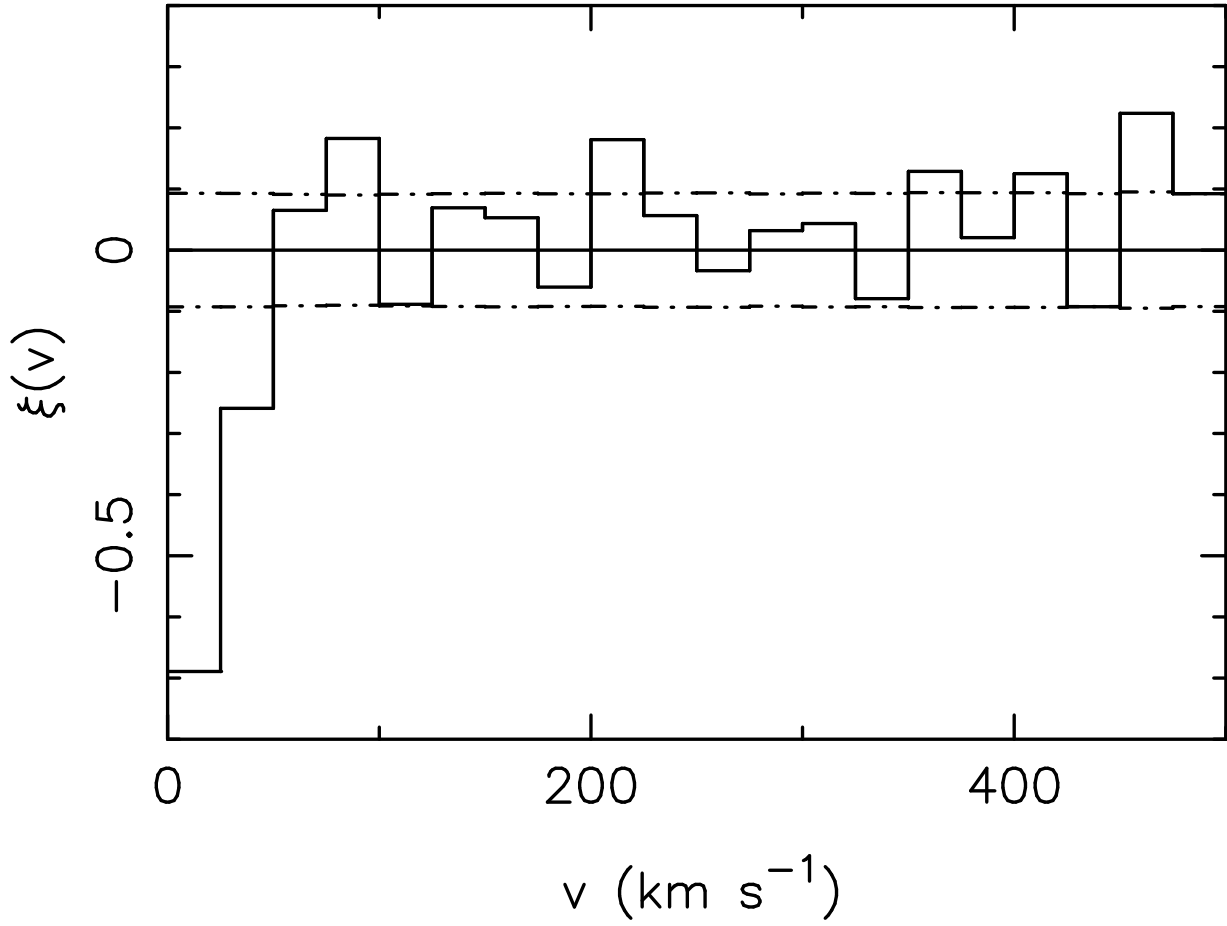


Fig. 15.— The two point correlation function for the 466 Ly $\alpha$  forest lines in the spectrum of HS 1946+7658. The bin size is 25 km s $^{-1}$ . The dashed line is the 1  $\sigma$  error array. The decrease at  $v < 50$  km s $^{-1}$  is due to line blending and blanketing.

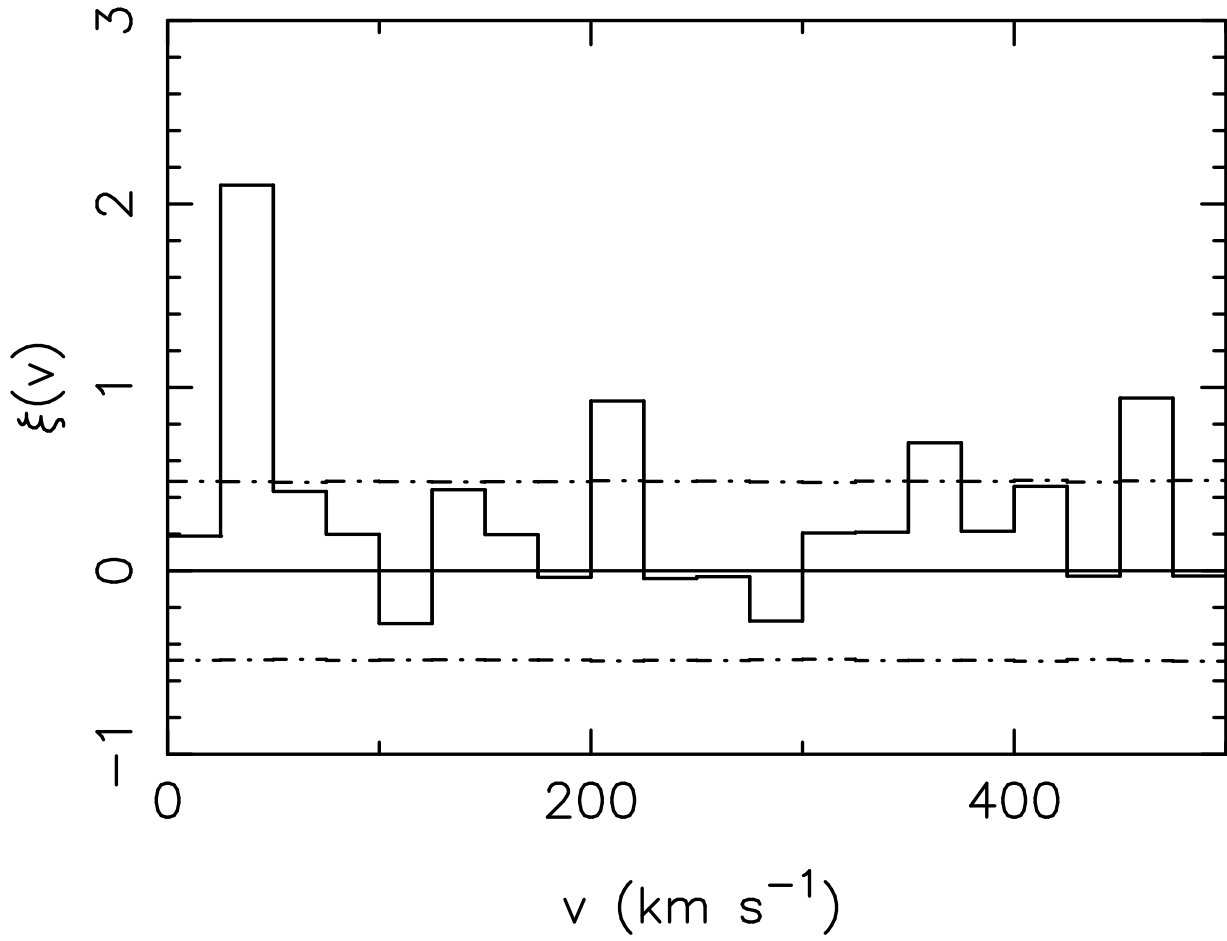


Fig. 16.— The two point correlation function for only the 120 Ly $\alpha$  forest lines in the spectrum of HS 1946+7658 with  $N(\text{H I}) > 10^{13.5}$ . The bin size is 25 km s<sup>-1</sup>. The dashed line is the 1  $\sigma$  error array.

TABLE 1  
 ABSORBERS WITH LINES BETWEEN 4170 Å AND 4923 Å.

$z$	$\log N$ ( $\text{cm}^{-2}$ )	$b$ ( $\text{km s}^{-1}$ )	$\sigma_z$	$\sigma_N$	$\sigma_b$	Ion	$\lambda$ observed (Å)
1.119017	12.02	5.6	0.000002	0.02	0.4	FeII	4767.53, 4790.63, 4967.43
1.738178	14.36	2.8	0.000001	0.03	0.5	FeII	4350.11, 4404.23, 4411.75
1.738179	14.51	2.7	0.000001	0.01	0.3	SiII	4180.40, 4950.66
1.738201	12.95	7.5	0.000003	0.02	0.6	NiII	4664.27, 4681.23, 4768.71, 4797.08
1.738242	12.16	1.2	0.000009	0.15	4.3	C IV	4239.33, 4246.38
1.738249	14.12	12.4	0.000013	0.06	1.1	FeII	4350.22, 4404.34, 4411.87
1.738253	14.43	11.3	0.000003	0.02	0.3	SiII	4180.51, 4950.80
1.738434	13.64	8.8	0.000002	0.02	0.3	C IV	4239.63, 4246.68
1.738750	13.35	50.5	0.000367	0.40	21.1	C IV	4240.12, 4247.17
1.738799	12.64	7.0	0.000013	0.15	2.4	C IV	4240.19, 4247.25
1.738970	13.09	9.0	0.000007	0.08	1.4	C IV	4240.46, 4247.51
2.176945	12.35	9.2	0.000014	0.09	1.9	C IV	4918.53, 4926.71
2.177267	13.42	15.6	0.000007	0.03	1.0	C IV	4919.03, 4927.21
2.177533	13.04	13.1	0.000013	0.06	1.1	C IV	4919.44, 4927.22
2.430432	12.79	38.7	0.000046	0.06	6.4	H I	4170.27
2.431397	13.16	27.3	0.000013	0.02	1.8	H I	4171.45
2.432004	12.05	7.6	0.000023	0.13	3.6	H I	4172.18
2.432759	12.58	19.3	0.000023	0.06	3.1	H I	4173.10
2.433959	12.99	61.3	0.000060	0.05	9.6	H I	4174.56
2.434924	12.52	17.8	0.000027	0.10	3.9	H I	4175.73
2.435871	12.74	10.1	0.000012	0.07	1.8	H I	4176.89
2.437110	14.35	107.0	0.000031	0.02	2.1	H I	4178.39
2.437501	14.72	41.6	0.000012	0.07	2.3	H I	4178.87
2.439909	12.35	10.3	0.000015	0.09	2.3	H I	4181.79
2.440449	12.87	86.9	0.000205	0.14	31.8	H I	4182.45
2.441634	12.67	33.2	0.000039	0.14	6.7	H I	4183.89
2.443398	12.54	26.9	0.000034	0.06	4.4	H I	4186.04
2.444537	13.38	32.7	0.000008	0.01	1.0	H I	4187.42
2.446516	12.84	24.4	0.000021	0.04	2.7	H I	4189.83
2.446887	12.65	2.1	0.000000	0.00	0.0	H I	4190.28
2.447371	12.89	33.6	0.000026	0.04	4.7	H I	4190.87
2.448151	13.01	19.1	0.000009	0.02	1.2	H I	4191.81
2.449207	13.26	38.5	0.000019	0.02	2.5	H I	4193.10
2.449861	12.86	15.9	0.000025	0.12	2.9	H I	4193.89
2.450512	14.29	31.9	0.000006	0.02	1.2	H I	4194.68
2.451230	12.31	10.5	0.000026	0.25	4.7	H I	4195.56
2.451527	12.58	22.7	0.000217	0.57	22.5	H I	4195.92
2.452268	12.91	35.2	0.000054	0.13	8.9	H I	4196.82
2.453455	13.15	69.5	0.000070	0.07	12.9	H I	4198.26
2.454392	12.33	8.5	0.000014	0.10	2.3	H I	4199.40
2.454814	12.48	15.3	0.000023	0.08	3.5	H I	4199.91
2.455357	13.02	20.4	0.000011	0.03	1.6	H I	4200.57
2.456718	14.33	55.0	0.000018	0.02	1.0	H I	4202.23
2.457301	14.15	21.0	0.000020	0.07	1.5	H I	4202.94
2.458956	12.53	25.4	0.000029	0.05	3.8	H I	4204.95
2.461935	12.81	76.6	0.000178	0.12	16.9	H I	4208.57
2.462547	14.18	26.2	0.000004	0.02	0.6	H I	4209.31
2.465350	14.47	37.3	0.000004	0.02	0.7	H I	4212.72
2.466931	13.50	45.3	0.000036	0.04	3.6	H I	4214.64
2.467542	13.40	21.9	0.000012	0.04	1.3	H I	4215.39
2.468674	13.66	32.5	0.000008	0.01	1.0	H I	4216.76
2.469697	12.94	37.9	0.000034	0.04	4.6	H I	4218.01
2.477774	12.58	56.5	0.000077	0.09	14.9	H I	4227.83
2.479035	13.23	34.0	0.000012	0.02	1.5	H I	4229.36
2.480487	13.10	25.9	0.000012	0.02	1.4	H I	4231.12
2.481605	12.57	56.4	0.000115	0.12	21.4	H I	4232.48
2.482701	13.75	22.2	0.000004	0.01	0.5	H I	4233.82
2.483460	12.91	26.5	0.000017	0.03	2.3	H I	4234.74
2.485171	13.25	30.5	0.000009	0.01	1.0	H I	4236.82
2.488367	12.27	45.7	0.000093	2.64	52.2	H I	4240.70
2.491472	13.09	135.4	0.000310	0.11	33.2	H I	4244.48
2.492775	12.91	39.6	0.000037	0.12	6.6	H I	4246.06
2.493941	13.42	40.2	0.000047	0.10	2.4	H I	4247.48
2.499261	13.96	59.6	0.000029	0.03	3.3	H I	4253.95
2.500453	13.67	50.5	0.000079	0.03	4.5	H I	4255.40
2.500761	13.79	23.1	0.000007	0.04	1.1	H I	4255.77
2.503897	13.28	39.6	0.000012	0.01	1.5	H I	4259.58
2.505207	13.10	33.6	0.000016	0.02	2.3	H I	4261.17
2.506100	13.36	25.0	0.000007	0.01	0.8	H I	4262.26
2.510810	13.05	21.9	0.000016	0.04	1.8	H I	4267.99
2.511514	12.51	32.7	0.000086	0.17	16.5	H I	4268.84
2.512310	12.86	22.4	0.000022	0.05	2.7	H I	4269.81
2.514674	13.61	17.4	0.000006	0.04	0.9	H I	4272.68
2.514841	13.61	35.5	0.000015	0.03	0.9	H I	4272.89
2.516700	13.69	22.8	0.000012	0.03	0.8	H I	4275.15
2.517205	13.73	25.0	0.000012	0.02	1.2	H I	4275.76
2.518199	13.28	34.1	0.000027	0.05	2.4	H I	4276.97
2.518341	12.98	15.2	0.000010	0.11	1.9	H I	4277.14

TABLE 1—*Continued*

$z$	$\log N$ ( $\text{cm}^{-2}$ )	$b$ ( $\text{km s}^{-1}$ )	$\sigma_z$	$\sigma_N$	$\sigma_b$	Ion	$\lambda$ observed ( $\text{\AA}$ )
2.519686	13.16	20.2	0.000012	0.05	1.1	H I	4278.78
2.520182	12.82	33.9	0.000081	0.11	7.1	H I	4279.38
2.521379	13.11	20.4	0.000008	0.02	0.9	H I	4280.83
2.522179	12.91	35.2	0.000104	0.16	11.2	H I	4281.81
2.522607	13.18	18.2	0.000008	0.07	1.2	H I	4282.33
2.523797	12.69	32.0	0.000031	0.05	4.2	H I	4283.77
2.524590	12.64	24.4	0.000024	0.05	3.5	H I	4284.74
2.525620	13.33	41.7	0.000010	0.01	1.3	H I	4285.99
2.526699	11.88	5.8	0.000017	0.10	2.6	H I	4287.30
2.527430	12.61	13.8	0.000012	0.06	1.6	H I	4288.19
2.527979	12.95	35.1	0.000027	0.03	3.3	H I	4288.86
2.529363	12.48	23.0	0.000022	0.05	2.8	H I	4290.54
2.530846	13.13	60.0	0.000235	0.21	13.2	H I	4292.34
2.530885	13.65	20.4	0.000027	0.07	1.6	H I	4292.39
2.531169	13.20	3.6	0.000010	0.29	2.6	H I	4292.74
2.531279	13.75	18.7	0.000028	0.09	1.9	H I	4292.87
2.532133	12.99	27.9	0.000026	0.11	4.9	H I	4293.91
2.532868	12.93	34.8	0.000037	0.09	7.3	H I	4294.80
2.533723	12.64	26.0	0.000076	0.21	9.6	H I	4295.84
2.534286	13.36	23.4	0.000055	0.18	4.6	H I	4296.53
2.534639	13.07	22.8	0.000107	0.30	4.8	H I	4296.95
2.536021	14.25	25.4	0.000005	0.01	0.4	H I	4298.63
2.536996	14.55	28.4	0.000091	0.24	3.0	H I	4299.82
2.538848	13.25	41.2	0.000266	0.64	28.4	H I	4302.07
2.539898	13.34	55.1	0.001610	2.13	192.9	H I	4303.35
2.540590	13.11	37.1	0.000146	1.92	16.9	H I	4304.19
2.541696	13.06	32.3	0.000014	0.02	1.7	H I	4305.53
2.543132	14.15	37.5	0.000003	0.01	0.4	H I	4307.28
2.545650	13.01	21.5	0.000040	0.15	2.6	H I	4310.34
2.546096	13.64	31.2	0.000025	0.04	1.7	H I	4310.88
2.548934	12.07	7.7	0.000015	0.07	2.1	H I	4314.33
2.549859	13.17	34.5	0.000013	0.02	1.5	H I	4315.46
2.550967	12.81	46.7	0.000045	0.04	5.9	H I	4316.80
2.553180	12.59	32.2	0.000061	0.12	6.5	H I	4319.49
2.554418	13.34	61.8	0.000066	0.07	10.8	H I	4321.00
2.555247	13.46	26.1	0.000009	0.04	1.6	H I	4322.01
2.555852	12.48	16.7	0.000031	0.09	3.6	H I	4322.74
2.556976	12.63	24.6	0.000027	0.05	3.4	H I	4324.11
2.559127	13.05	61.0	0.000031	0.02	3.9	H I	4326.72
2.561354	13.28	74.3	0.000087	0.06	5.5	H I	4329.43
2.561902	14.27	25.5	0.000002	0.01	0.5	H I	4330.10
2.564085	12.79	59.5	0.000073	0.06	9.6	H I	4332.75
2.565132	14.10	21.3	0.000015	0.05	0.7	H I	4334.02
2.565858	14.37	37.7	0.000021	0.16	5.2	H I	4334.91
2.566277	13.77	55.1	0.000565	0.64	18.4	H I	4335.42
2.569966	13.21	39.9	0.000073	0.13	3.5	H I	4339.90
2.570569	12.80	16.1	0.000010	0.13	2.3	H I	4340.63
2.570810	13.00	51.9	0.000310	0.28	18.0	H I	4340.93
2.572638	13.05	14.5	0.000005	0.05	0.9	H I	4343.15
2.572869	12.89	44.8	0.000203	0.14	14.0	H I	4343.43
2.573364	13.22	19.2	0.000006	0.06	1.3	H I	4344.03
2.574936	13.82	19.8	0.000002	0.01	0.3	H I	4345.94
2.575315	13.16	111.3	0.000087	0.04	14.4	H I	4346.40
2.576901	13.67	23.7	0.000017	0.04	1.0	H I	4348.33
2.577307	13.45	23.3	0.000026	0.06	1.4	H I	4348.82
2.579328	12.78	114.7	0.000141	0.07	23.8	H I	4351.28
2.581100	12.86	24.6	0.000035	0.08	3.1	H I	4353.44
2.581774	13.53	19.8	0.000028	0.26	3.0	H I	4354.26
2.582206	13.72	19.4	0.000019	0.21	3.0	H I	4354.78
2.582346	13.87	42.6	0.000207	0.27	8.2	H I	4354.95
2.583694	13.30	22.6	0.000005	0.01	0.6	H I	4356.59
2.585053	13.42	20.9	0.000006	0.04	1.1	H I	4358.24
2.585142	13.58	47.1	0.000011	0.03	1.6	H I	4358.35
2.593012	13.29	34.4	0.000009	0.01	1.0	H I	4367.92
2.595320	12.98	83.6	0.000062	0.03	7.5	H I	4370.72
2.598567	13.53	34.3	0.000007	0.01	0.8	H I	4374.67
2.599294	12.66	40.1	0.000160	0.22	16.6	H I	4375.55
2.600860	12.36	13.1	0.000019	0.10	2.9	H I	4377.46
2.600911	13.23	76.5	0.000040	0.02	5.8	H I	4377.52
2.603406	12.43	23.2	0.000028	0.05	3.4	H I	4380.55
2.604458	13.58	22.3	0.000003	0.01	0.3	H I	4381.83
2.605196	12.49	16.1	0.000015	0.04	1.9	H I	4382.73
2.605831	12.02	13.5	0.000032	0.10	4.2	H I	4383.50
2.606853	12.41	20.8	0.000023	0.05	2.8	H I	4384.74
2.609690	12.40	29.3	0.000093	0.14	9.3	H I	4388.19
2.610233	13.51	19.2	0.000004	0.01	0.4	H I	4388.85
2.612296	13.69	33.8	0.000003	0.00	0.3	H I	4391.36
2.614778	12.55	53.5	0.000066	0.09	10.4	H I	4394.38
2.615181	13.11	17.3	0.000011	0.05	1.0	H I	4394.87
2.615936	13.89	33.6	0.000131	0.20	7.2	H I	4395.78
2.616275	13.96	20.1	0.000016	0.16	2.5	H I	4396.20
2.617090	13.81	24.1	0.000004	0.01	0.4	H I	4397.19



TABLE 1—*Continued*

$z$	$\log N$ ( $\text{cm}^{-2}$ )	$b$ ( $\text{km s}^{-1}$ )	$\sigma_z$	$\sigma_N$	$\sigma_b$	Ion	$\lambda$ observed ( $\text{\AA}$ )
2.618476	12.62	59.0	0.000072	0.06	9.6	H I	4398.87
2.620016	12.50	13.1	0.000029	0.09	2.7	H I	4400.74
2.620298	12.15	10.9	0.000047	0.20	4.6	H I	4401.09
2.621883	13.65	43.4	0.000176	0.21	6.7	H I	4403.01
2.621980	13.33	16.0	0.000017	0.16	2.3	H I	4403.13
2.622709	13.92	29.1	0.000177	2.90	27.0	H I	4404.02
2.623015	13.49	39.3	0.005184	8.01	210.2	H I	4404.39
2.623839	12.98	24.0	0.000078	0.40	8.5	H I	4405.39
2.624329	12.60	16.4	0.000036	0.25	5.7	H I	4405.99
2.624830	13.60	28.8	0.000010	0.02	1.5	H I	4406.60
2.627541	13.15	55.2	0.000018	0.01	2.1	H I	4409.89
2.633091	12.97	30.2	0.000013	0.02	1.5	H I	4416.64
2.637402	13.97	34.7	0.000008	0.01	0.7	H I	4421.88
2.638135	12.81	23.2	0.000044	0.19	6.2	H I	4422.77
2.638802	13.07	37.1	0.000044	0.13	11.0	H I	4423.58
2.639987	14.01	25.5	0.000006	0.03	1.0	H I	4425.02
2.640301	13.25	59.7	0.000231	0.20	12.5	H I	4425.40
2.642595	13.59	66.5	0.000813	0.63	36.5	H I	4428.19
2.643061	15.23	29.0	0.000005	0.09	1.1	H I	4428.76
2.644779	14.97	48.7	0.000005	0.02	0.7	H I	4430.85
2.647517	14.24	46.0	0.000022	0.02	1.1	H I	4434.18
2.648620	14.83	39.3	0.000015	0.03	0.7	H I	4435.52
2.651372	12.76	28.1	0.000070	0.14	4.5	H I	4438.86
2.651695	13.69	20.7	0.000005	0.02	0.5	H I	4439.26
2.652345	12.33	15.3	0.000028	0.10	3.9	H I	4440.05
2.652966	13.26	26.6	0.000028	0.10	3.0	H I	4440.80
2.653944	13.88	28.0	0.000016	0.08	3.4	H I	4441.99
2.654377	14.36	70.5	0.000050	0.04	2.3	H I	4442.52
2.656856	13.82	21.5	0.000002	0.01	0.3	H I	4445.53
2.657153	13.31	76.2	0.000035	0.02	3.8	H I	4445.89
2.659214	12.69	41.1	0.000109	0.13	10.6	H I	4448.40
2.659972	13.33	28.3	0.000016	0.05	2.3	H I	4449.32
2.660658	13.54	31.7	0.000013	0.02	1.4	H I	4450.15
2.661663	12.89	33.3	0.000019	0.03	2.4	H I	4451.37
2.662823	13.13	22.1	0.000005	0.01	0.6	H I	4452.78
2.665816	12.61	22.7	0.000062	0.13	4.3	H I	4456.42
2.666225	12.36	6.8	0.000007	0.16	1.9	H I	4456.92
2.666373	12.80	23.9	0.000071	0.14	4.7	H I	4457.10
2.667900	12.64	52.9	0.000393	0.34	26.0	H I	4458.96
2.668562	13.09	29.1	0.000048	0.18	6.7	H I	4459.76
2.669027	13.85	19.6	0.000005	0.02	0.4	H I	4460.33
2.669928	12.97	26.8	0.000009	0.02	1.2	H I	4461.42
2.671090	13.30	43.6	0.000009	0.01	1.2	H I	4462.83
2.672241	13.65	19.5	0.000002	0.01	0.2	H I	4464.23
2.673298	13.03	80.1	0.000055	0.03	7.0	H I	4465.52
2.676373	13.41	74.6	0.000015	0.02	2.8	H I	4469.26
2.676388	12.96	23.3	0.000009	0.05	1.6	H I	4469.27
2.678944	12.90	30.2	0.000010	0.01	1.2	H I	4472.38
2.682106	13.32	25.9	0.000007	0.03	1.0	H I	4476.23
2.682723	12.48	16.3	0.000021	0.18	3.4	H I	4476.98
2.683239	13.50	106.0	0.000076	0.07	8.0	H I	4477.60
2.683250	12.93	17.2	0.000007	0.10	2.1	H I	4477.62
2.683919	12.54	15.7	0.000017	0.13	3.1	H I	4478.43
2.684876	12.38	8.1	0.000018	0.13	1.7	H I	4479.59
2.685110	12.20	13.0	0.000061	0.20	6.1	H I	4479.88
2.687225	12.50	28.1	0.000035	0.05	4.3	H I	4482.45
2.688236	13.22	20.6	0.000005	0.03	0.9	H I	4483.68
2.689964	12.56	53.5	0.001059	0.98	84.0	H I	4485.78
2.690899	14.63	34.8	0.000010	0.03	1.8	H I	4486.92
2.691736	13.69	27.3	0.000025	0.05	1.5	H I	4487.93
2.692694	13.60	21.4	0.000003	0.01	0.3	H I	4489.10
2.695102	13.29	19.3	0.000003	0.01	0.3	H I	4492.02
2.695968	12.26	26.1	0.000052	0.09	7.0	H I	4493.08
2.696618	12.36	20.6	0.000030	0.07	3.5	H I	4493.87
2.698569	12.61	45.1	0.000043	0.04	5.6	H I	4496.24
2.699691	12.89	28.0	0.000012	0.02	1.5	H I	4497.60
2.700739	12.92	26.0	0.000027	0.05	2.4	H I	4498.88
2.701429	13.50	29.7	0.000008	0.02	1.6	H I	4499.72
2.702116	13.65	21.0	0.000004	0.01	0.4	H I	4500.55
2.702584	12.23	39.4	0.000132	0.18	13.8	H I	4501.12
2.705060	12.48	34.3	0.000030	0.04	3.6	H I	4504.13
2.706571	13.87	30.1	0.000004	0.01	0.4	H I	4505.97
2.707257	12.89	26.1	0.000025	0.05	2.2	H I	4506.80
2.709160	12.08	23.8	0.000050	0.09	6.1	H I	4509.11
2.710135	13.62	34.6	0.000003	0.00	0.4	H I	4510.30
2.712504	12.91	29.6	0.000008	0.01	1.0	H I	4513.18
2.718247	12.79	23.6	0.000008	0.02	1.0	H I	4520.16
2.719359	12.94	25.5	0.000007	0.01	0.9	H I	4521.51
2.720383	13.20	29.6	0.000005	0.01	0.6	H I	4522.76
2.721750	12.46	21.6	0.000016	0.03	1.7	H I	4524.42
2.724251	12.69	37.5	0.000049	0.07	4.1	H I	4527.46
2.725220	12.60	51.6	0.000110	0.10	10.8	H I	4528.64

TABLE 1—*Continued*

$z$	$\log N$ ( $\text{cm}^{-2}$ )	$b$ ( $\text{km s}^{-1}$ )	$\sigma_z$	$\sigma_N$	$\sigma_b$	Ion	$\lambda$ observed ( $\text{\AA}$ )
2.727370	13.43	23.7	0.000003	0.01	0.4	H I	4531.25
2.728187	13.21	91.9	0.000058	0.02	4.0	H I	4532.25
2.728841	12.68	14.5	0.000007	0.03	1.0	H I	4533.04
2.731698	13.38	19.9	0.000003	0.01	0.3	H I	4536.51
2.732606	13.55	22.0	0.000002	0.01	0.3	H I	4537.62
2.734689	12.44	41.0	0.000095	0.13	14.3	H I	4540.15
2.735744	12.76	38.1	0.000043	0.05	4.8	H I	4541.43
2.737072	12.48	15.2	0.000020	0.12	2.7	H I	4543.05
2.737994	13.87	18.8	0.000010	0.05	1.6	H I	4544.17
2.738028	14.13	48.8	0.000009	0.02	2.2	H I	4544.21
2.738760	13.53	79.6	0.000145	0.10	7.1	H I	4545.10
2.740802	13.00	22.0	0.000007	0.01	0.9	H I	4547.58
2.741658	13.36	27.1	0.000005	0.01	0.6	H I	4548.62
2.742620	13.09	26.1	0.000007	0.01	0.8	H I	4549.79
2.743792	13.44	24.2	0.000003	0.01	0.3	H I	4551.22
2.746888	12.76	44.1	0.000023	0.02	2.6	H I	4554.98
2.748594	12.57	25.3	0.000015	0.03	1.8	H I	4557.05
2.749815	12.75	41.6	0.000021	0.02	2.5	H I	4558.54
2.751263	12.01	15.1	0.000027	0.08	3.6	H I	4560.30
2.751639	11.77	5.7	0.000016	0.12	2.6	H I	4560.75
2.752212	12.49	31.0	0.000027	0.05	3.9	H I	4561.45
2.754030	12.63	86.7	0.000259	0.15	31.8	H I	4563.66
2.755317	12.60	43.0	0.000051	0.14	7.3	H I	4565.23
2.756356	12.37	20.5	0.000019	0.05	2.5	H I	4566.49
2.757303	13.04	38.5	0.000010	0.01	1.2	H I	4567.64
2.758289	12.05	22.8	0.000049	0.09	6.5	H I	4568.84
2.759613	13.46	20.8	0.000012	0.08	1.6	H I	4570.45
2.759816	13.99	38.0	0.000011	0.02	0.6	H I	4570.70
2.760753	12.57	14.8	0.000015	0.18	2.5	H I	4571.83
2.761395	14.02	24.9	0.000002	0.05	1.1	H I	4572.62
2.762716	13.21	67.1	0.003106	2.30	183.6	H I	4574.22
2.763146	14.20	30.4	0.000074	0.26	5.2	H I	4574.74
2.763361	13.48	16.7	0.000050	0.50	6.9	H I	4575.01
2.764058	12.82	22.4	0.000052	1.76	31.9	H I	4575.85
2.764717	12.46	14.7	0.000083	1.00	11.3	H I	4576.65
2.764910	12.77	53.2	0.001644	1.61	141.6	H I	4576.89
2.765907	13.55	23.5	0.000005	0.03	0.7	H I	4578.10
2.767069	12.89	70.5	0.000090	0.11	8.6	H I	4579.51
2.769052	11.78	9.8	0.000029	0.11	3.8	H I	4581.92
2.770139	12.03	14.5	0.000028	0.08	3.5	H I	4583.24
2.771040	12.80	29.9	0.000016	0.02	1.9	H I	4584.34
2.772435	13.26	27.7	0.000014	0.02	1.2	H I	4586.04
2.772693	12.18	3.9	0.000009	0.12	2.1	H I	4586.35
2.773374	13.18	33.3	0.000018	0.03	2.7	H I	4587.18
2.774065	12.52	16.4	0.000056	0.63	8.3	H I	4588.02
2.774611	12.71	19.5	0.000069	0.90	12.9	H I	4588.68
2.774844	13.18	45.3	0.000428	0.45	19.8	H I	4588.96
2.776313	13.03	24.8	0.000036	0.07	2.4	H I	4590.75
2.777391	14.85	37.5	0.000005	0.05	1.5	H I	4592.06
2.778547	13.92	27.2	0.000008	0.01	0.7	H I	4593.47
2.779492	12.17	23.4	0.000058	0.12	8.9	H I	4594.62
2.780167	12.39	41.6	0.000075	0.08	9.7	H I	4595.44
2.782453	12.78	71.0	0.000056	0.03	7.2	H I	4598.21
2.784085	12.11	32.5	0.000086	0.12	10.2	H I	4600.20
2.785307	13.27	23.7	0.000004	0.01	0.5	H I	4601.68
2.786984	12.53	18.9	0.000018	0.04	2.3	H I	4603.72
2.790152	12.18	16.5	0.000021	0.05	2.5	H I	4607.57
2.791111	13.46	30.5	0.000003	0.00	0.4	H I	4608.74
2.792892	12.91	94.2	0.000061	0.03	7.7	H I	4610.91
2.796026	12.42	25.2	0.000026	0.05	3.6	H I	4614.71
2.796962	12.50	26.3	0.000023	0.04	2.9	H I	4615.85
2.798168	12.84	48.9	0.000025	0.02	3.1	H I	4617.32
2.800346	13.89	41.4	0.000002	0.00	0.2	H I	4619.97
2.803018	12.88	83.0	0.000389	0.21	20.9	H I	4623.21
2.803428	12.53	26.4	0.000035	0.25	6.8	H I	4623.71
2.804509	12.57	33.9	0.000070	0.20	8.6	H I	4625.03
2.805540	13.18	28.9	0.000006	0.01	0.7	H I	4626.28
2.806742	12.22	31.3	0.000044	0.06	5.4	H I	4627.74
2.809386	12.48	40.4	0.000030	0.03	3.5	H I	4630.96
2.811019	13.46	34.6	0.000010	0.02	0.5	H I	4632.94
2.811218	13.01	16.4	0.000006	0.05	1.0	H I	4633.18
2.817860	14.09	27.3	0.000054	0.12	1.4	H I	4641.26
2.818131	13.74	19.6	0.000043	0.30	4.4	H I	4641.59
2.818545	13.74	27.1	0.000037	0.06	1.8	H I	4642.09
2.819816	12.90	50.7	0.000024	0.02	3.0	H I	4643.64
2.821543	12.32	25.4	0.000035	0.06	4.1	H I	4645.74
2.822665	13.91	36.7	0.000006	0.01	0.6	H I	4647.10
2.823326	12.94	19.1	0.000015	0.12	2.4	H I	4647.90
2.823796	13.14	41.6	0.000073	0.07	5.1	H I	4648.47
2.826045	12.36	30.1	0.000035	0.05	3.9	H I	4651.21
2.827651	13.22	31.8	0.000007	0.01	0.8	H I	4653.16
2.828738	14.48	22.3	0.000002	0.02	0.3	H I	4654.48

TABLE 1—*Continued*

$z$	$\log N$ ( $\text{cm}^{-2}$ )	$b$ ( $\text{km s}^{-1}$ )	$\sigma_z$	$\sigma_N$	$\sigma_b$	Ion	$\lambda$ observed ( $\text{\AA}$ )
2.830004	13.60	21.6	0.000004	0.02	0.6	H I	4656.02
2.830272	13.31	50.8	0.000039	0.04	2.1	H I	4656.35
2.831872	12.27	23.6	0.000047	0.08	5.5	H I	4658.29
2.843362	12.43	11.1	0.000037	0.14	2.1	SiII	4575.20, 4586.25, 4844.26
2.844026	12.38	4.2	0.000022	0.16	2.2	SiII	4575.99, 4587.04, 4845.1
2.844169	12.49	3.6	0.000017	0.21	3.5	SiII	4576.16, 4587.21, 4845.27
2.844288	14.20	2.1	0.000004	0.60	0.7	SiII	4576.30, 4587.35, 4845.43
2.844295	13.27	3.4	0.000001	0.01	0.2	FeII	4216.72, 4253.17, 4313.20, 4326.55, 4332.90, 4358.14, 4391.59, 4394.90, 4401.48, 4845.86
2.844315	12.54	4.2	0.000003	0.05	0.4	N I	4611.45, 4614.04, 4615.91
2.844368	12.91	5.3	0.000037	0.27	2.3	SiII	4576.40, 4587.45, 4845.53
2.845063	11.63	4.9	0.000020	0.31	3.3	SiII	4577.22, 4588.28, 4846.40
2.845289	12.45	12.5	0.000018	0.06	2.1	SiII	4577.49, 4588.54, 4846.69
2.884011	14.37	34.2	0.000011	0.04	2.3	H I	4721.68
2.884506	14.08	76.3	0.000191	0.11	7.2	H I	4722.28
2.885299	13.15	19.8	0.000010	0.05	1.2	H I	4723.24
2.885533	13.31	24.4	0.000003	0.01	0.3	H I	4727.17
2.890091	12.83	40.2	0.000087	0.09	5.7	H I	4729.07
2.890906	12.90	32.2	0.000029	0.14	8.0	H I	4730.06
2.891370	12.53	14.8	0.000018	0.17	3.1	H I	4730.62
2.892821	16.76	35.5	0.000002	0.04	0.3	H I	4732.39
2.894939	13.19	19.3	0.000002	0.01	0.3	H I	4734.96
2.896250	12.33	24.6	0.000020	0.03	2.3	H I	4736.55
2.899562	12.55	41.7	0.000034	0.03	4.1	H I	4740.58
2.900227	11.57	9.2	0.000031	0.20	4.7	H I	4741.39
2.901063	11.98	18.8	0.000035	0.08	4.3	H I	4742.41
2.901690	13.19	17.4	0.000003	0.01	0.4	H I	4743.17
2.902339	13.00	31.1	0.000011	0.02	1.7	H I	4743.96
2.903116	12.60	14.3	0.000024	0.18	2.0	H I	4744.90
2.903418	12.84	21.7	0.000052	0.10	3.2	H I	4745.27
2.904207	12.32	62.0	0.000040	0.10	17.8	H I	4746.23
2.905904	12.39	40.5	0.000043	0.05	5.7	H I	4748.29
2.906983	13.52	20.9	0.000001	0.00	0.2	H I	4749.60
2.909543	13.05	47.6	0.000351	0.36	12.9	H I	4752.71
2.909847	13.84	24.7	0.000003	0.05	0.8	H I	4753.08
2.910390	12.37	15.4	0.000025	0.27	3.6	H I	4753.74
2.911078	12.61	26.9	0.000024	0.04	2.2	H I	4754.58
2.912376	12.16	31.6	0.000039	0.05	4.4	H I	4756.16
2.914462	13.55	44.3	0.000010	0.01	0.8	H I	4758.69
2.915339	13.69	31.4	0.000004	0.01	0.4	H I	4759.76
2.917112	15.39	42.7	0.000001	0.01	0.2	H I	4761.92
2.919066	12.63	36.8	0.000018	0.03	2.5	H I	4764.29
2.921112	13.53	35.7	0.000003	0.01	0.4	H I	4766.78
2.921582	13.10	132.4	0.000109	0.03	14.2	H I	4767.35
2.923492	12.57	30.4	0.000017	0.02	1.9	H I	4769.67
2.925363	11.81	14.8	0.000030	0.11	3.8	H I	4771.95
2.927119	13.57	77.0	0.000058	0.04	3.6	H I	4774.08
2.927163	13.89	24.5	0.000020	0.04	0.9	H I	4774.13
2.927684	13.99	25.2	0.000016	0.04	1.8	H I	4774.77
2.928244	12.63	20.1	0.000081	0.23	4.8	H I	4775.45
2.929193	12.95	41.2	0.000021	0.03	2.7	H I	4776.60
2.930221	13.03	23.1	0.000005	0.01	0.5	H I	4777.85
2.931926	13.34	36.6	0.000042	0.14	1.8	H I	4779.92
2.932066	13.83	25.4	0.000006	0.05	0.8	H I	4780.09
2.934067	12.89	33.0	0.000014	0.02	1.6	H I	4782.53
2.934781	12.27	17.9	0.000021	0.06	2.5	H I	4783.40
2.935612	12.26	20.4	0.000039	0.17	4.2	H I	4784.41
2.936216	12.59	38.3	0.000081	0.08	6.9	H I	4785.14
2.938102	12.16	30.7	0.000054	0.09	6.4	H I	4787.43
2.939288	12.85	46.7	0.000022	0.02	2.5	H I	4788.87
2.942197	13.16	42.3	0.000014	0.01	1.4	H I	4792.41
2.943192	13.28	29.2	0.000006	0.01	0.9	H I	4793.62
2.944010	14.03	22.4	0.000002	0.00	0.2	H I	4794.61
2.944584	12.35	32.5	0.000055	0.08	5.5	H I	4795.31
2.946747	12.63	94.9	0.000110	0.05	13.4	H I	4797.94
2.948354	13.18	34.5	0.000005	0.01	0.7	H I	4799.90
2.949535	12.76	29.8	0.000028	0.05	2.6	H I	4801.33
2.950266	12.21	29.4	0.000086	0.18	11.6	H I	4802.22
2.950968	12.23	16.3	0.000038	0.32	4.6	H I	4803.07
2.951411	12.01	29.4	0.000316	0.63	40.9	H I	4803.61
2.952037	11.57	14.3	0.000083	0.42	9.4	H I	4804.37

TABLE 1—*Continued*

$z$	$\log N$ ( $\text{cm}^{-2}$ )	$b$ ( $\text{km s}^{-1}$ )	$\sigma_z$	$\sigma_N$	$\sigma_b$	Ion	$\lambda$ observed ( $\text{\AA}$ )
2.952849	12.60	28.8	0.000012	0.02	1.5	H I	4805.36
2.954315	12.33	50.8	0.000095	0.08	8.2	H I	4807.14
2.954830	12.14	23.8	0.000029	0.05	3.2	H I	4807.77
2.955936	12.74	26.9	0.000009	0.02	1.1	H I	4809.11
2.957044	13.16	39.7	0.000015	0.02	1.7	H I	4810.46
2.957367	12.24	6.2	0.000005	0.02	0.6	H I	4810.85
2.957832	12.36	12.5	0.000025	0.21	2.6	H I	4811.42
2.958167	12.59	20.1	0.000048	0.13	5.7	H I	4811.82
2.959043	12.60	27.4	0.000011	0.04	1.8	H I	4812.89
2.959912	12.01	18.7	0.000023	0.11	3.6	H I	4813.95
2.961081	12.63	24.6	0.000008	0.03	1.2	H I	4815.37
2.963002	13.15	207.3	0.000283	0.03	24.5	H I	4817.70
2.963982	13.32	18.9	0.000002	0.01	0.3	H I	4818.89
2.964278	12.98	56.8	0.000038	0.05	3.6	H I	4819.25
2.964689	12.40	5.7	0.000003	0.03	0.5	H I	4819.75
2.964944	11.86	1.7	0.000005	0.05	1.7	H I	4820.06
2.965544	12.44	6.2	0.000003	0.02	0.4	H I	4820.79
2.967993	12.90	30.8	0.000019	0.03	1.5	H I	4823.77
2.968666	13.30	25.0	0.000005	0.01	0.5	H I	4824.59
2.969375	11.74	16.5	0.000035	0.11	4.9	H I	4825.45
2.970534	12.43	21.3	0.000012	0.02	1.4	H I	4826.86
2.971254	12.07	22.5	0.000028	0.05	3.4	H I	4827.73
2.973089	12.90	27.8	0.000007	0.01	0.8	H I	4829.97
2.974059	13.17	26.5	0.000004	0.01	0.4	H I	4831.14
2.975993	12.36	25.6	0.000020	0.03	2.2	H I	4833.50
2.978110	13.77	25.4	0.000001	0.00	0.1	H I	4836.07
2.978975	12.88	25.4	0.000006	0.01	0.7	H I	4837.12
2.982135	11.91	35.7	0.000114	0.13	13.6	H I	4840.96
2.983498	13.63	35.4	0.000056	0.10	1.3	H I	4842.62
2.983663	13.56	20.9	0.000009	0.11	1.7	H I	4842.82
2.984988	15.55	26.7	0.000008	0.08	0.8	H I	4844.43
2.986302	13.30	44.3	0.000202	0.40	42.8	H I	4846.03
2.986915	13.26	20.2	0.000031	0.28	4.6	H I	4846.77
2.987395	13.53	33.5	0.000045	0.06	3.0	H I	4847.36
2.989719	13.34	21.9	0.000003	0.01	0.3	H I	4850.18
2.990526	12.52	23.5	0.000017	0.03	2.2	H I	4851.16
2.991674	13.41	33.3	0.000005	0.01	0.6	H I	4852.56
2.992723	14.22	27.2	0.000003	0.01	0.4	H I	4853.83
2.993391	13.40	51.5	0.000094	0.08	6.6	H I	4854.65
2.994458	11.85	14.2	0.000032	0.20	5.1	H I	4855.94
2.995774	12.17	23.4	0.000087	0.22	5.6	H I	4857.54
2.996401	13.42	32.7	0.000010	0.01	1.1	H I	4858.30
2.997403	12.98	27.8	0.000007	0.01	0.9	H I	4859.52
2.998347	12.30	21.3	0.000015	0.03	1.8	H I	4860.67
2.999553	12.89	35.5	0.000049	0.06	3.4	H I	4862.14
3.000190	13.06	24.5	0.000012	0.05	1.9	H I	4862.91
3.000831	13.20	23.6	0.000008	0.03	1.2	H I	4863.69
3.001493	12.19	27.6	0.000080	0.24	14.5	H I	4864.49
3.002269	13.34	27.0	0.000005	0.01	0.5	H I	4865.44
3.003692	12.37	31.5	0.000019	0.03	2.3	H I	4867.17
3.005095	12.69	23.8	0.000009	0.02	1.0	H I	4868.87
3.005824	12.85	21.4	0.000011	0.04	1.2	H I	4869.76
3.006546	13.02	36.3	0.000021	0.06	5.4	H I	4870.64
3.007355	13.77	27.1	0.000004	0.02	0.6	H I	4871.62
3.008333	13.42	51.9	0.000319	0.32	27.2	H I	4872.81
3.008956	14.75	25.9	0.000002	0.01	0.6	H I	4873.57
3.010144	12.84	42.0	0.000055	0.05	3.6	H I	4875.01
3.011800	12.82	30.7	0.000006	0.01	0.7	H I	4877.02
3.013830	12.59	40.9	0.000142	0.32	9.5	H I	4879.49
3.014380	12.42	16.3	0.000015	0.14	2.1	H I	4880.16
3.015070	13.62	26.4	0.000003	0.04	1.1	H I	4881.00
3.015500	13.54	90.1	0.000192	0.10	7.7	H I	4881.52
3.015999	13.17	19.0	0.000005	0.02	0.6	H I	4882.13
3.021789	13.70	18.2	0.000015	0.09	1.1	H I	4889.17
3.022060	14.18	28.3	0.000013	0.02	0.4	H I	4889.50
3.022955	13.33	23.6	0.000003	0.01	0.3	H I	4890.59
3.023952	11.96	17.2	0.000020	0.05	2.4	H I	4891.80
3.026462	13.03	67.8	0.001172	0.89	35.2	H I	4894.85
3.026761	13.67	27.1	0.000073	0.59	5.8	H I	4895.21
3.027356	14.06	42.6	0.000119	0.52	38.3	H I	4895.94
3.027913	13.91	23.0	0.000053	0.27	3.8	H I	4896.61
3.028278	13.89	24.4	0.000062	0.17	1.9	H I	4897.06
3.029714	14.14	21.1	0.000009	0.03	0.3	H I	4898.80
3.030113	13.77	23.9	0.000025	0.05	0.9	H I	4899.29
3.031546	12.45	16.1	0.000015	0.04	1.3	H I	4901.03
3.032089	13.60	21.7	0.000002	0.01	0.2	H I	4901.69
3.032568	12.80	40.8	0.000042	0.05	3.5	H I	4902.27
3.034015	13.49	21.8	0.000012	0.11	1.4	H I	4904.03
3.034360	13.93	33.5	0.000028	0.04	1.1	H I	4904.45
3.035417	13.15	24.5	0.000004	0.01	0.4	H I	4905.74
3.038455	14.45	33.0	0.000002	0.01	0.2	H I	4909.43
3.039506	12.41	27.7	0.000038	0.10	7.1	H I	4910.71

TABLE 1—*Continued*

$z$	$\log N$ ( $\text{cm}^{-2}$ )	$b$ ( $\text{km s}^{-1}$ )	$\sigma_z$	$\sigma_N$	$\sigma_b$	Ion	$\lambda$ observed ( $\text{\AA}$ )
3.040076	12.40	13.0	0.000011	0.05	1.2	H I	4911.40
3.042059	12.45	33.4	0.000024	0.03	2.6	H I	4913.81
3.045177	13.40	32.9	0.000004	0.00	0.4	H I	4917.60
3.047379	13.21	66.9	0.000042	0.03	5.2	H I	4920.28
3.048303	13.56	19.9	0.000015	0.04	0.9	H I	4921.40
3.049432	12.25	12.7	0.000024	0.08	1.0	SiII	4820.51, 4832.51
3.049457	13.33	14.2	0.000014	0.05	0.6	C II	4196.6
3.049511	13.19	4.0	0.000002	0.05	0.5	C II	4196.66
3.049516	12.25	3.5	0.000002	0.06	0.6	SiII	4820.61, 4832.25
3.049589	14.28	10.3	0.000016	0.18	1.7	S IV	4303.34
3.049714	17.38	32.8	0.000004	0.03	0.2	H I	4922.96
3.049784	11.91	6.2	0.000006	0.05	1.0	SiII	4820.93, 4832.57
3.049796	12.83	6.4	0.000007	0.06	1.1	C II	4196.95
3.049888	14.23	7.5	0.000013	0.33	2.6	S IV	4303.66
3.050070	13.69	2.3	0.000021	0.33	4.4	S IV	4303.86
3.050079	11.69	7.5	0.000007	0.04	1.1	SiII	4821.28, 4832.92
3.050083	12.74	8.9	0.000007	0.04	1.3	C II	4197.25
3.050190	13.75	3.3	0.000025	0.51	4.9	S IV	4303.98
3.050375	13.40	6.2	0.000001	0.01	0.2	C II	4197.55
3.050377	12.53	5.8	0.000001	0.00	0.1	SiII	4821.63
3.050435	14.32	8.4	0.000012	0.13	1.5	S IV	4304.24